The Optimal Selection of Submerged Vanes Geometric Dimensions in Curved Channels with Sediment Flow

Parisa Rezaei [1], Elham Fazel Najafabadi [*,1], Mohammad Shayannejad [1]

1. Department of Water Science and Engineering. College of Agriculture, Isfahan University of Technology, Isfahan, Iran.

***Corresponding Author:**
Elham Fazel Najafabadi,

Email: efazel@iut.ac.ir
Received: 2025.05.07
Accepted: 2025.06.23
J. Hydraul. Struct., 12(2):74-102
DOI: 10.22055/jhs.2025.49586.1349

ABSTRACT

One of the major challenges in diverting water from rivers is the intrusion of sediment into intakes, which can cause operational issues and damage infrastructure. Various methods have been explored to mitigate this problem, including the use of submerged vanes. This study employed simulations to evaluate the effectiveness of submerged vanes and the impact of their geometric parameters on reducing sediment inflow. Results showed the sediment transport estimation error for the optimal computational mesh size (2.7cm × 1cm) was 0.55%. The findings indicated that the optimal vane height and length were 0.5 times the flow depth and 2.5 times the vane height, respectively. Additionally, the optimal transverse and longitudinal spacing between vanes, as well as the distance from the nearest vane row to the intake wall, were determined to be 2.17, 5, and 2 times the vane height, respectively. Flow analysis showed that near the bed, the maximum velocity cores were directed toward the outer bend and the intake, whereas at the water surface, these cores became more widely distributed across the channel. Negative vertical velocities were concentrated at the intake entrance. In the absence of submerged vanes, the maximum secondary flow strength was found near the bed across the full channel width. However, when vanes were present, the strongest secondary currents shifted to the left side of the vanes.

KEYWORDS
Sediment discharge, Water intake, Curved channel, Geometric parameters, Simulation.

1. Introduction

The continuous growth of the global population and industrial development has significantly increased water demand. On the other hand, declining water resources and rising pollution levels have become major concerns for water resource engineers. Among the most accessible sources of water are surface waters, particularly rivers. Understanding river behavior and sediment transport—especially in meandering sections—is crucial for effective river engineering.

One common method of water diversion for industrial, agricultural, and municipal uses involves the use of lateral intake channels branching from the main river flow. However, along with the diverted water, mobile sediment also enters these lateral channels and is transported to pumping stations, treatment plants, and farmland. This sediment intrusion can lead to a range of physical, hydraulic, and environmental problems.

As a result, controlling and reducing sediment entry into lateral intakes has become a key focus in hydraulic engineering over recent decades. Various methods and structural solutions have been proposed to mitigate sediment intrusion. These include the use of skimming walls [e.g., 1-4], spur dikes [e.g., 5-8], permeable and impermeable groynes [e.g., 9-12], dikes [13, 14], and submerged vanes. Although the use of these structures has been mainly aimed at reducing transported sediment, their use can also be mentioned with a focus on flow structure [15, 16] and reducing scour around the bridge pier [17, 18, 19].

Submerged vanes are among the most commonly employed sediment control structures to the intakes, designed to mitigate sediment intrusion effectively. Beyond their role in sediment management, these structures have proven valuable in various critical riverine environments for both flow regulation and sediment control. For instance, in areas with complex flow patterns, submerged vanes can be utilized to reduce local scour around hydraulic structures such as bridge piers—submerged vanes often placed in straight river sections due to structural or stability constraints [20, 21, 22, 23]. Moreover, the accumulation of floating woody debris—resulting from factors such as flooding and deforestation—presents a significant challenge to hydraulic infrastructure, including the submerged vanes [24]. Despite these broader applications, the present study is specifically focused on evaluating the effectiveness of submerged screens in reducing sediment inflow into reservoirs.

Submerged vanes are one of the most widely used methods of preventing and reducing sediments entering the lateral channels in research. Odgaard was one of the first researchers in the field of the use of submerged vanes, and by conducting his laboratory research from 1983 to 2009, he provided one of the most comprehensive research projects in the field of submerged vanes.

Following other laboratory, field and numerical researches such as Odgaard and Lee [25] and Odgaard and Mosconi [26], Odgaard and Wang [27], Barkdoll et al. [28], Marelius and Sinha [29], Gupta et al. [30], Tan et al. [31], Ouyang [32], Sharma et al. [33], Karami et al. [34], Biswas and Barbhuiya [35]. In line with the specific application of submerged vanes to control and reduce the sediment input to the lateral channels, many researches have been done, including Nakato et al. [36], Raudkivi [37], Wang et al. [38], Ouyang [39], Ho et al. [40], Michel et al. [41], Sarhadi and Jabbarri [42].

Tseng et al. [43] conducted their study in a quasi-field-scale laboratory channel, where permeable vanes were installed next to one of the channel walls under live-bed conditions dominated by bed load transport, with negligible suspended sediment.

Estimates of bed load transport along the channel showed that the vanes were effective in redirecting sediment laterally. Under laboratory conditions, the maximum rate of lateral sediment transfer ranged from 9% to 18% of the total average stream-wise transport within the domain. Mhsen and Hilo [44] investigated the installation angle of submerged vanes under various discharge conditions. Their results indicated that a 20-degree angle was most effective in deflecting sediment. The optimal performance of submerged vanes was observed when the lateral channel discharge was less than 20% of the total flow.

Hilo [45] developed a physical model comprising a main channel, a lateral sub-channel, and a sediment feeding mechanism to reduce sediment entry into the sub-channel and redistribute sediment flow. The results indicated that vane performance was more effective at lower flow rates, with a 20-degree installation angle identified as optimal. Aminian et al. [46] examined the impact of submerged vanes positioned at angles of 30°, 45°, and 60° relative to the main flow direction on sediment diversion into a 90-degree lateral channel. Their findings revealed that increasing the Froude number by 0.3 led to a 22.2% reduction in

diverted water discharge and a 53.3% reduction in diverted sediment load. Additionally, the study concluded that under lower Froude numbers and shallower flow depths, a 30-degree vane angle offers the most effective sediment diversion performance.

Chauhan et al. [47] reviewed recent advances in sediment diversion using submerged vanes, highlighting current limitations and offering suggestions for future research. Their study provided a detailed analytical foundation on the physics governing vane performance and thoroughly examined design parameters through analytical relationships. Additionally, the paper reviewed various applications of submerged vanes and proposed a research agenda to enhance riverine navigation through improved vane implementation. In a separate study, Gumgum et al. [48] conducted 26 experimental tests to evaluate the impact of submerged vane parameters and discharge ratios on bed erosion and morphology at a 90-degree lateral channel. Their findings identified the vane deviation angle and water discharge ratio as the most influential factors affecting erosion, while other parameters showed minimal effects within the tested range. The optimal configuration, offering the highest efficiency, was achieved with a vane angle of 45 degrees.

Bor [49] conducted experiments to analyze three-dimensional flow patterns and sediment distribution over a mobile bed in the presence of submerged vanes during sediment inflow. The study concluded that a row of three submerged vanes could reduce sediment diversion by approximately 20%. Baltazar et al. [50] carried out experimental investigations on the role of submerged vanes in limiting sediment entry into a 90-degree lateral channel. Their findings indicated that in the presence of submerged vanes, the circulating current is not formed in the main channel, thereby reducing bed load transfer to the lateral intake by about 75%. Additionally, submerged vanes increased the flow separation zone within the lateral intake and generated higher levels of turbulence kinetic energy. Kalathil et al. [51] examined the effect of collars and submerged vanes on reducing sediment ingress into lateral channels. Their results showed the lowest performance at a vane angle of 15 degrees, with a 46.82% reduction in sediment, and the highest at 40 degrees, achieving an 85.36% reduction compared to conditions without vanes. The study also found that collars enhanced vane performance at 40 degrees and were effective in reducing sediment diversion at 15 degrees when the collar diameter was three times the vane height.

Serajian et al. [52] conducted experiments in a converging arc with a 90-degree angle to investigate the effects of channel convergence, submerged vane angle, and Froude number on sediment diversion. Their findings indicated that while an increase in the Froude number leads to greater sediment diversion, the installation of submerged vanes reduces it. Among the tested configurations, vanes installed at the smallest angle (25 degrees) were most effective in minimizing sediment entry into the lateral channel. Karami Moghadam et al. [53] carried out laboratory tests using submerged vanes and lateral channels with a 55-degree angle, examining both round-edged and sharp-edged intake openings. Vanes were arranged in a zigzag pattern at angles of 10 and 30 degrees relative to the flow. Results showed that round-edged openings increased scouring while decreasing sediment inflow to the lateral channel. In another study, Karmi et al. [34] calibrated a three-dimensional Computational Fluid Dynamics (CFD) model with experimental data to assess flow patterns, discharge deviation ratios, secondary flow intensities, and vortex structures. Their results demonstrated that increasing the narrowing ratio of the channel reduces diverted flow, while greater longitudinal spacing between vanes intensifies the velocity gradient, causing more severe bed erosion near the vanes.

A review of previous studies reveals that most existing research has been primarily experimental, with limited use of numerical

methods for parameter optimization. Moreover, prior optimization efforts have largely focused on the dimensions of submerged vanes, often within a narrow range of values. In light of these gaps, the present study aimed to optimize both the geometric characteristics of submerged vanes—specifically their length and height—as well as their longitudinal and transverse spacing, including the distance between the first row of vanes and the intake. The objective function for all optimization scenarios was to minimize the sediment inflow rate into the water intake.

Materials and Methods

In this study, the SSIIM software was employed as a numerical solver of the Navier–Stokes equations to simulate three-dimensional flow patterns and sediment deviation at the entrance of a diversion channel. SSIIM is well-suited for sediment-related studies, capable of simulating both suspended and bed load transport, including non-uniform sediment distributions. The software supports modeling of complex sediment processes such as sorting, armoring, and bed stratification—features that often require significant customization in more generic CFD platforms. Additionally, SSIIM2 facilitates the simulation of morphological changes in riverbeds, intakes, and reservoirs through its ability to use multiblock and nested block grids, reducing the need for extensive user intervention or advanced coding.

Governing equations

The fundamental governing equations used in the simulation are the continuity and momentum equations. The continuity equation, expressed in Cartesian coordinates (x, y, z) and assuming constant fluid density, is given as follows:

$$V_f \frac{\partial \rho}{\partial t} + \frac{\partial}{\partial x}(\rho u A_x) + \frac{\partial}{\partial y}(\rho v A_y) + \frac{\partial}{\partial z}(\rho u w) = 0 \quad (1)$$

Here, V_F denotes the flow volume fraction; ρ is the fluid density; t represents time; u, v, and w are the velocity components in the x, x, and x directions, respectively; and A_x, A_y, and A_z represent the surface flow fractions in the respective directions. Equation (2) presents the momentum equations in three dimensions:

$$\begin{aligned}
\frac{\partial u}{\partial t} + \frac{1}{V_F}\left\{uA_x\frac{\partial u}{\partial x} + vA_y\frac{\partial u}{\partial y} + wA_z\frac{\partial u}{\partial z}\right\} &= -\frac{1}{\rho}\frac{\partial P}{\partial x} + Gr_x + Vi_x \\
\frac{\partial u}{\partial t} + \frac{1}{V_F}\left\{uA_x\frac{\partial u}{\partial x} + vA_y\frac{\partial u}{\partial y} + wA_z\frac{\partial u}{\partial z}\right\} &= -\frac{1}{\rho}\frac{\partial P}{\partial x} + Gr_x + Vi_x \\
\frac{\partial w}{\partial t} + \frac{1}{V_F}\left\{uA_x\frac{\partial w}{\partial x} + vA_y\frac{\partial w}{\partial y} + wA_z\frac{\partial w}{\partial z}\right\} &= -\frac{1}{\rho}\frac{\partial P}{\partial z} + Gr_z + Vi_z
\end{aligned} \quad (2)$$

where Gr_x, Gr_y, and Gr_z are the accelerations caused by gravity; and Vi_x, Vi_y, and Vi_z are the accelerations caused by viscosity in the x, y, and z directions, respectively.

Sediment transport is composed of two components: bed load and suspended load. The suspended load is calculated using the convective-diffusion equation based on sediment concentration:

$$\frac{\partial c}{\partial t} + U_j\frac{\partial c}{\partial x_j} + \omega\frac{\partial c}{\partial z} = \frac{\partial c}{\partial x_j}\left(\Gamma_T\frac{\partial c}{\partial x_j}\right) \quad (3)$$

Where ω is the sediment fall velocity, x Cartesian distance, and Γ_T is the dispersion coefficient, which can be calculated as follows:

$$\Gamma_T = \frac{\vartheta_T}{S_C} \quad (4)$$

ν_T is the Eddy viscosity and S_c is the Schmidt number, which varies in the range of 0.7-1 [54].

Additionally, the numerical model applies

the van Rijn [55] equation to calculate the bed load transport within the layer between the bed surface and the foundation surface.

Turbulence modeling

The SSIIM software is designed to support a variety of turbulence models, including the standard k-ε model, the RNG-enhanced k-ε model, a localized k-ε model based on wind shear, the Spalart-Allmaras model, and two versions of the k-ω model—one incorporating Wilcox's wall laws and the other utilizing k-ε wall laws. Since the software is available in two versions (SSIIM 1 and SSIIM 2), the availability of specific turbulence models may vary between them. Comparative evaluation against laboratory experiments indicated that the RNG k-ε model yields the most accurate results. Therefore, this study primarily employed the standard k-ε model. The standard k-ε model is a widely adopted two-equation turbulence model, where one equation governs the turbulent kinetic energy (k) and the other governs its dissipation rate (ε) [56]. These governing equations are expressed as follows [57]:

$$\frac{\partial}{\partial t}(\rho k)+\frac{\partial}{\partial x_i}(\rho k u_i) = \frac{\partial}{\partial x_i}\left[(\mu+\frac{\mu_t}{\sigma_k})\frac{\partial k}{\partial x_i}\right] + G_k + G_b - \rho\varepsilon - Y_M + S_k \quad (5)$$

$$\frac{\partial}{\partial t}(\rho \varepsilon)+\frac{\partial}{\partial x_i}(\rho \varepsilon u_i) = \frac{\partial}{\partial x_j}\left[(\mu+\frac{\mu_t}{\sigma_\varepsilon})\frac{\partial \varepsilon}{\partial x_j}\right] + C_{1\varepsilon}\frac{\varepsilon}{k}(G_k + C_{3\varepsilon}G_b) - C_{2\varepsilon}\rho\frac{\varepsilon^2}{k} + S_\varepsilon \quad (6)$$

$$\mu_t = \rho C_\mu \frac{k^2}{\varepsilon} \quad (7)$$

In these equations, G_b and G_k represent the production of turbulent kinetic energy due to buoyancy and velocity gradients, respectively. The term Y_M accounts for the contribution of compressibility to the production of turbulence. The constants $C_{1\varepsilon}$, $C_{2\varepsilon}$, $C_{3\varepsilon}$, and C_μ are empirical coefficients with typical values of 1.44, 1.92, 0.09, and 0.09, respectively. S_k and S_ε are the turbulent Prandtl numbers for k and ε, typically taken as 1.0 and 1.3, respectively. μ_t denotes the eddy viscosity.

Boundary conditions and gridding

In this study, the flow field was simulated using SSIIM2, employing two computational blocks: one for the main channel and one for the lateral intake. The main channel consisted of two straight sections—upstream and downstream—connected by a 180-degree bend. For the hydraulic boundary conditions, the discharge and cross-sectional flow area were specified at the upstream and downstream ends, respectively. Sediment-related input parameters, including particle size, sediment type, and fall velocity, were also provided to the software for sediment transport calculations. Since SSIIM2 does not independently support the complex meshing required for this geometry, auxiliary tools such as AutoCAD, MATLAB, and Excel were used to generate the computational mesh. The mesh density was adapted to the significance of different regions, with finer mesh elements placed near the submerged vanes and coarser elements at the channel's inlet and outlet. Based on the main channel width, intake width, and vane positioning, a grid resolution of 2.7 × 1 cm was selected in the longitudinal and transverse directions, respectively. The computational domain included 235 longitudinal sections, 34 transverse sections, and 11 vertical layers, which were imported into SSIIM2 for simulation.

The boundary conditions for the main mesh block included specified inflow discharge, water depth, and the Manning–Strickler roughness coefficient at the channel entrance; an outflow condition at the downstream end; and wall boundaries applied to the channel bed and sidewalls. For the diversion channel, boundary conditions included symmetry at the

entrance and upper boundary, outflow at the exit, and wall conditions for all remaining surfaces.

Model verification

The numerical simulation was verified using experimental data from Shirali et al. [58]. In that study, a rectangular main channel with a relative curvature of R/B = 4.7 was used. The intake was positioned at a 120° angle along the outer arc of the bend, with an intake alignment angle of 70°. Eight submerged vanes were installed in the main channel, arranged in two longitudinal rows of four, positioned opposite the intake (Fig. 1). The main channel inflow rate was 20 L/s, with a water depth of 12 cm and a Froude number of 0.26. The intake flow rate was measured at 4.27 L/s.

To validate the simulation results and mesh quality, the output from the SSIIM software (after reaching convergence) was compared with the experimental results of Shirali et al. [58]. Upon identifying discrepancies attributed to the mesh resolution, the mesh was refin ed, and the simulations were rerun. The optimal mesh was selected when the results from two consecutive simulations showed minimal variation, indicating mesh independence. The percentage error was calculated using the following formula:

$$\frac{|Predicted\ Sediment - Measured\ Sediment|}{Measured\ Sediment} \times 100 = \%\ ERROR \quad (8)$$

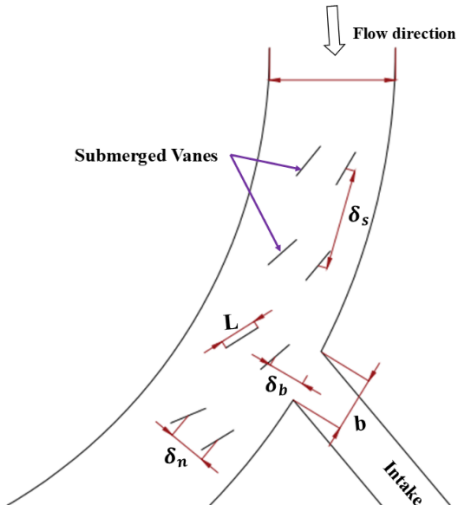


Figure 1. Position of submerged vanes in the channel

Parameter variations

In line with the stated objectives, this study investigated variations in five key parameters: vane height, vane length, longitudinal spacing between vanes, transverse spacing between vanes, and the distance of the first row of vanes from the water intake. The variation ranges for these parameters were selected based on the recommendations from Odgaard [59] and are summarized in Table 1.

In this table, H represents the height of

Table 1. Recommended and used range for parameters [59, 39]

Parameter	Recommended range	The range used
$H(cm)$	$0.2 \leq {}^{H}/_{y} \leq 0.4$	$0.5 \leq {}^{H}/_{y} \leq 0.2$
$L(cm)$	3H	$2H \leq L \leq 3H$
$\delta_s(cm)$	$10H \leq \delta_s \leq 30H$	$4H \leq \delta_s \leq 12H$
$\delta_n(cm)$	3H	$2H \leq \delta_n \leq 3H$
$\delta_b(cm)$	3H	3H

the submerged vanes, L is the length of the vanes, δ_s refers to the longitudinal spacing between vanes, $\delta_n$is the transverse spacing, and δ_b indicates the distance of the vanes from the intake. Throughout these parameter variations, the angle between the flow direction and the vanes, along with key hydraulic parameters such as flow depth and discharge, were kept constant.

The following steps were taken in this study:

a) *Vane Height Optimization:* In the first step, the height of the submerged vanes was varied between 3 and 6 cm to evaluate its effect on sediment inflow to the intake. The sediment discharge values obtained from SSIIM simulations were used as input to the PSO algorithm. The PSO algorithm, implemented in MATLAB, was then used to determine the optimal vane height.

b) *Vane Length Optimization:* After determining the optimal height, the vane length was varied between 12 and 18 cm (corresponding to 2 to 3 times the vane height). Sediment discharge results from SSIIM were again used as input to the MATLAB-based PSO algorithm to identify the optimal vane length.

c) *Spacing Optimization:* In the third step, spacing parameters were investigated. The transverse spacing between vanes was varied from 2 to 3 times the vane height (12–18 cm), longitudinal spacing from 4 to 12 times the vane height (24–72 cm), and the distance from the first vane row to the intake from 2 to 3 times the vane height (12–18 cm). Sixteen different scenarios were simulated to identify the optimal combination of spacing parameters.

3. Results and Discussion

3.1. Optimal mesh and sediment diversion efficiency to the side channel

To ensure simulations are accurate and reliable, the optimal mesh size was first determined. Meshes were categorized into five different classes regarding their grid dimensions (i×j): 5.4×2cm, 4.1×1.5cm, 3.5×1.25cm, 2.7×1cm, and 1.3×0.5cm. It is noteworthy that *i* values (5.4, 4.1, 3.5, 2.7, and 1.3 cm) correspond to the grid spacing along the flow direction, while the *j* values (2, 1.5, 1.25, 1, and 0.5 cm) show the spacing across the channel width. Among these configurations, Scenario 4—with a mesh dimension of 2.7×1cm, and sediment simulation error of less than 1%—was identified as optimal. Simulations were performed under flow conditions consisting of a 20 L/s discharge in the main channel, a 4.27 L/s intake flow rate, and a Froude number of 0.26.

The primary goal of the SSIIM simulations was to estimate both the sediment transport rate and the amount of sediment entering the intake. The optimal mesh was selected by comparing the SSIIM results for each mesh configuration against experimental data reported by Shirali et al. [58]. These comparative results are presented in Table 2. In this table, $\mathbf{Q_{SM}}$ denotes the sediment flow rate at the end of the main channel, while $\mathbf{Q_{SI}}$ refers to the sediment flow rate entering the water intake.

As can be seen, mesh refinement does not necessarily lead to optimal results. The reason for this can be stated as follows: One of the main limitations of the SSIIM software—and a significant challenge in mesh generation—is the restriction on the number of computational cells. Specifically, the grid dimensions in the *i* and *j* directions must not exceed 300 × 300 cells. Additionally, the number of cells in the *j* direction must remain constant along the entire channel length. During simulation, when the mesh is refined, especially near submerged vanes, the lack of compatibility

Table 2. Dimensions of meshing, review, and comparison of laboratory results with SSIIM software

No.	Cell Dimensions		Number of cells	$Q_{SM}+Q_{SI}$(gr/s)	Error %
	Longitude direction(cm)	Transverse direction(cm)			
1	5.4	2	60750	4189.52	5.81
2	4.1	1.5	66440	4265.95	4.09
3	3.5	1.25	72290	4344.13	2.33
4	2.7	1	78300	4423.43	0.55
5	1.3	0.5	117720	4896	10.09

between adjacent cells can lead to convergence problems, large numerical errors, or even cause the simulation to fail entirely. This limitation was evident in the simulation results: as the mesh resolution was increased from 1 cm to 0.5 cm, the network error (or result divergence) rose sharply.

3.2 Optimal values of parameters

According to the ranges provided in previous research, parameter values were considered for each parameter at each stage, and by keeping other parameters constant, a simulation was performed using SSIIM software. Thus, a total of 29 scenarios were defined and simulated (Table 3). Based on the proposed range parameters in previous studies, values were assigned to each parameter, and simulations were performed while keeping the others constant. In general, a total of 29 simulation scenarios were defined and executed (Table 3).

Table 3: Range of submerged vane heights investigated

Scenario	$H(cm)$	$L(cm)$	$\delta_n(cm)$	$\delta_s(cm)$	$\delta_b(cm)$	$Q_{SI}(\%)$
1	3	18	18	48	18	31.36
2	3.5	18	18	48	18	30.69
3	4	18	18	48	18	29.78
4	4.5	18	18	48	18	29.26
5	5	18	18	48	18	28.91
6	5.5	18	18	48	18	28.43
7	6	18	18	48	18	27.40
8	6	12	18	48	18	29.05
9	6	13.2	18	48	18	30.26
10	6	14.4	18	48	18	26.97
11	6	15.6	18	48	18	25.64
12	6	16.8	18	48	18	29.06
13	6	18	18	48	18	27.4
14	6	15	12	48	18	25.69
15	6	15	13.2	48	18	25.46
16	6	15	14.4	48	18	25.78
17	6	15	15.6	48	18	26.18
18	6	15	16.8	48	18	26.61
19	6	15	18	48	18	26.84
20	6	15	13	24	18	25.15
21	6	15	13	36	18	21.46
22	6	15	13	48	18	25.77

Scenario	$H(cm)$	$L(cm)$	$\delta_n(cm)$	$\delta_s(cm)$	$\delta_b(cm)$	$Q_{SI}(\%)$
23	6	15	13	60	18	23.13
24	6	15	13	72	18	23.93
25	6	15	13	30	12	14.8
26	6	15	13	30	13.2	16.31
27	6	15	13	30	14.4	17.53
28	6	15	13	30	15.6	19.57
29	6	15	13	30	16.8	20.38

The water depth in all simulations was fixed at 12 cm, and according to the inequality proposed by Odgaard [59], the height of the submerged vanes was set within the range of 3 to 6 cm (Scenarios 1–7). Considering the optimal depth value, Vane length values were evaluated between 12 and 18 cm (Scenarios 8–13). Similarly, with the optimal depth and length of vanes and according to Odgaard's suggestion, the vanes' transverse spacing was varied from 12 to 18 cm (Scenarios 14–19). Using the optimal values for vane height, length, and transverse spacing and regarding the recommendations of Odgaard [59] and Ouyang [39], longitudinal vane spacing was varied between 24 and 72 cm (Scenarios 20–24). Finally, considering the optimal four parameters mentioned, the distance from the intake to the first row of vanes was selected in the range of 12 to 18 cm (Scenarios 25–29), also in accordance with Odgaard's inequality.

The objective function of all simulations was to minimize the percentage of sediment entering the water intake. After each simulation, the percentage of sediment entering the intake was calculated as a proportion of the total transported sediment and recorded in Table 3. Results from the seven scenarios for vane height changes illustrated that increasing the height from 3 to 6 cm reduced sediment entering the intake from 31.36% to 27.40%—a 3.96% decrease. Both the SSIIM simulation and the PSO algorithm results identified a vane height of 6 cm as optimal, which was then used in subsequent simulations. Simulation results of decreasing vane lengths exhibited oscillatory behavior in performance. A minimum percentage of sediment entering the intake was observed at 15.6 cm in SSIIM simulations, while the PSO algorithm recommended a length of 15 cm as optimal length. This value was used for the next stages.

Increasing the transverse spacing from 12 to 13.2 cm caused a decreasing trend for the sediment entering the intake. However, beyond 13.2 cm, further increases of distance led to a decrease in vane effectiveness, with sediment entering the intake increasing to 26.84% at 18 cm. Thus, the lowest sediment entering the intake occurred at 13.2 cm, by 25.66%, while the PSO algorithm revealed an optimal spacing of 13 cm, which was selected for further analysis. Changes in the longitudinal space of vanes demonstrated an oscillatory pattern in sediment intake. Based on SSIIM results, the minimum sediment entering (21.46%) occurred at a longitudinal space of 36 cm, but the PSO algorithm recommended 30 cm as the optimal longitudinal distance. The different distances between the intake and the first vane row were also investigated. Results showed that as this distance increased from 12 to 18 cm, vane effectiveness decreased, and sediment intake increased from 14.8% to 21.98%. The PSO algorithm proposed 12 cm as the optimal distance.

3.3 Velocity Contours

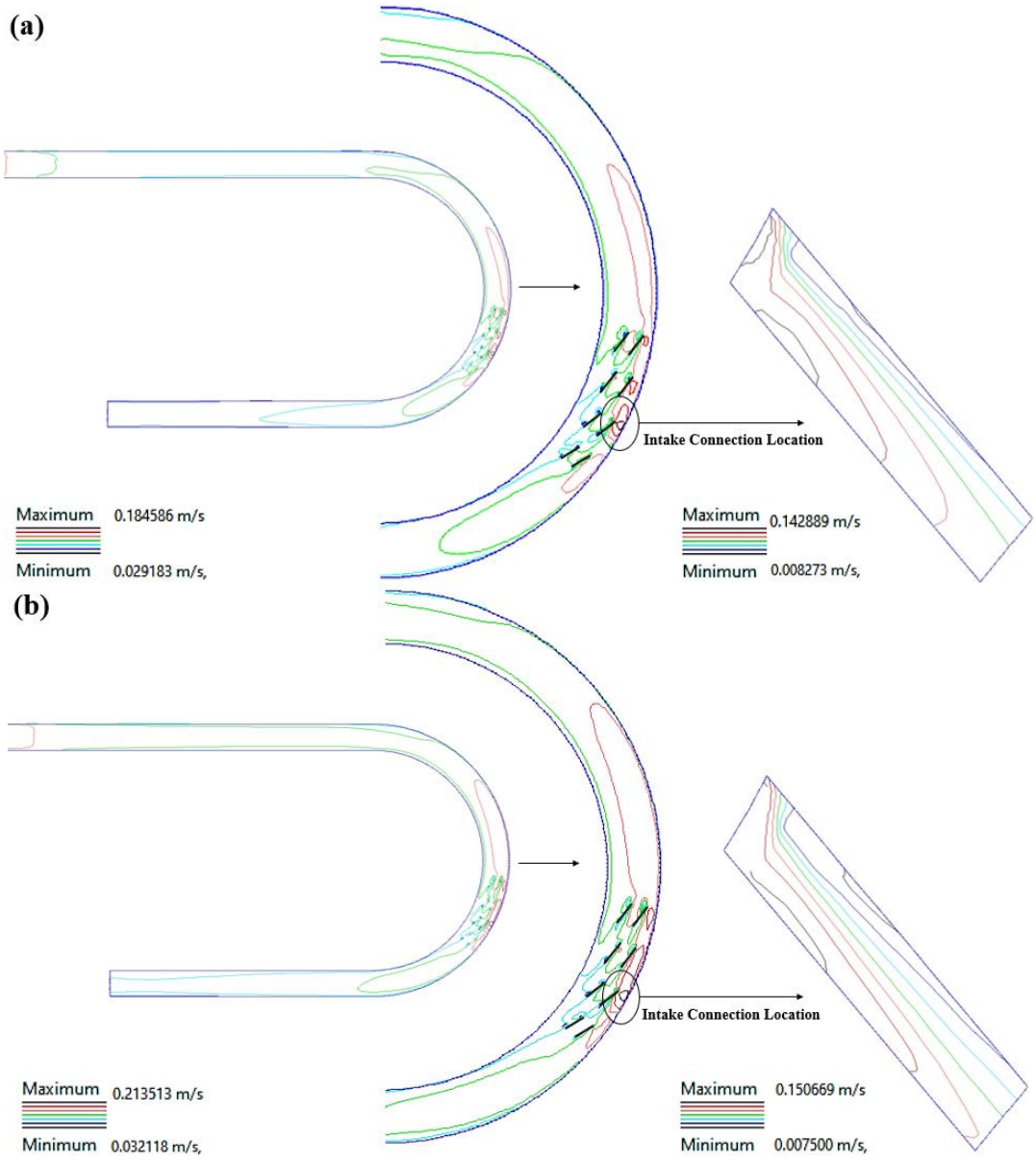
After determining the optimal values for the five parameters, in this stage, the horizontal and vertical velocity contour lines associated with each parameter were investigated. Due to the high similarity among the contour-line plots and the large

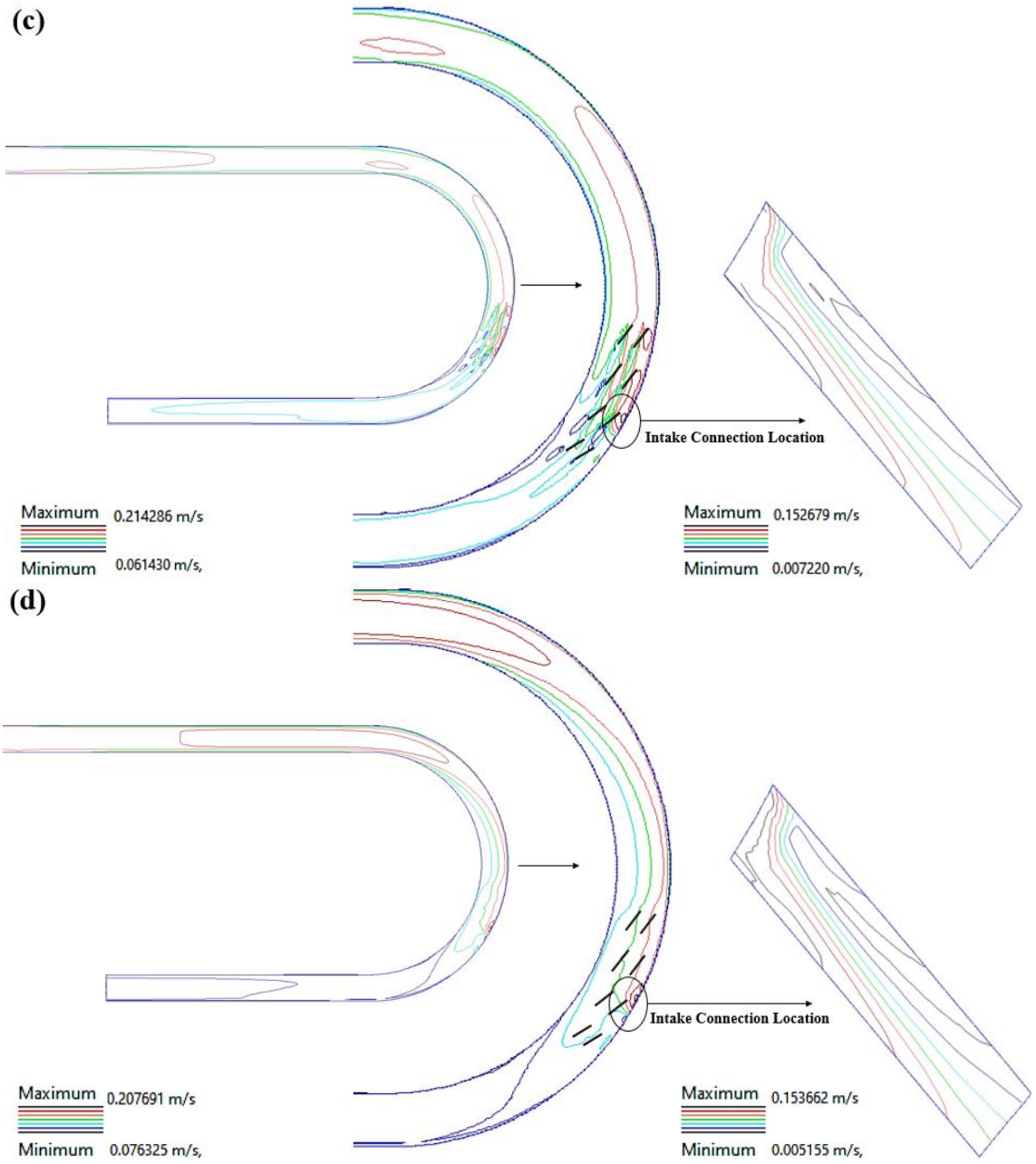
number of diagrams, only the contour lines related to the optimal vane height are presented in the main text. The other contour-line plots for the remaining scenarios are included in the appendix, while their explanations are provided in the main text. It should be noted that consistent depth levels were used across all stages of the analysis.

3.3.1 Vane Optimal Height

Figures 2 and 3 represent the streamwise and vertical velocity contour-line plots at five depth levels for a vane height of 6 cm. The mentioned levels include: (a) bed, (b) h/y = 0.3, (c) h/y = 0.6, (d) h/y = 0.8, and (e) h/y = 0.975, where *h* represents the vertical distance from the bed to the specified level.

The velocity variations displayed that by moving flow from the bed towards the water surface, the highest velocity gradients occur in the adjacent of submerged vanes and also the intake. As shown in Figure 2c, the flow above the submerged vanes remains influenced by the vane structures yet, and high stream wise velocity gradients are observed.




(c)
Intake Connection Location
Maximum 0.214286 m/s
Minimum 0.061430 m/s,
Maximum 0.152679 m/s
Minimum 0.007220 m/s,
(d)
Intake Connection Location
Maximum 0.207691 m/s
Minimum 0.076325 m/s,
Maximum 0.153662 m/s
Minimum 0.005155 m/s,

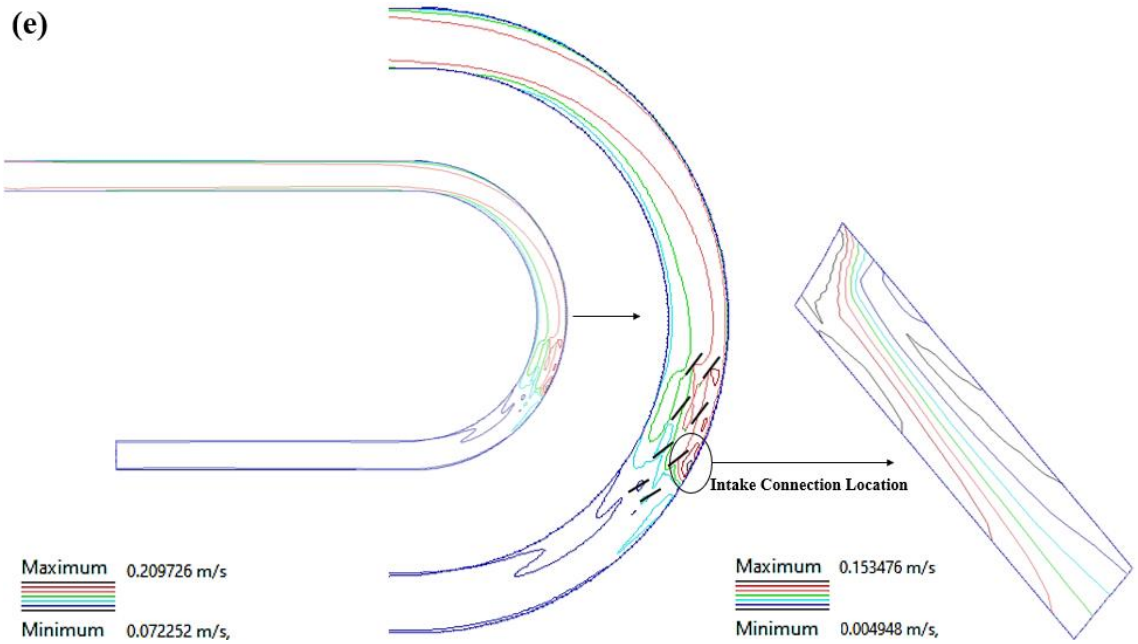


Figure 2. Stream-wise velocities in main channel and intake (Vane Height is 6cm) a) h/y=0, b) h/y=0.3, c) h/y=0.6, d) h/y=0.8, e) h/y=0.975

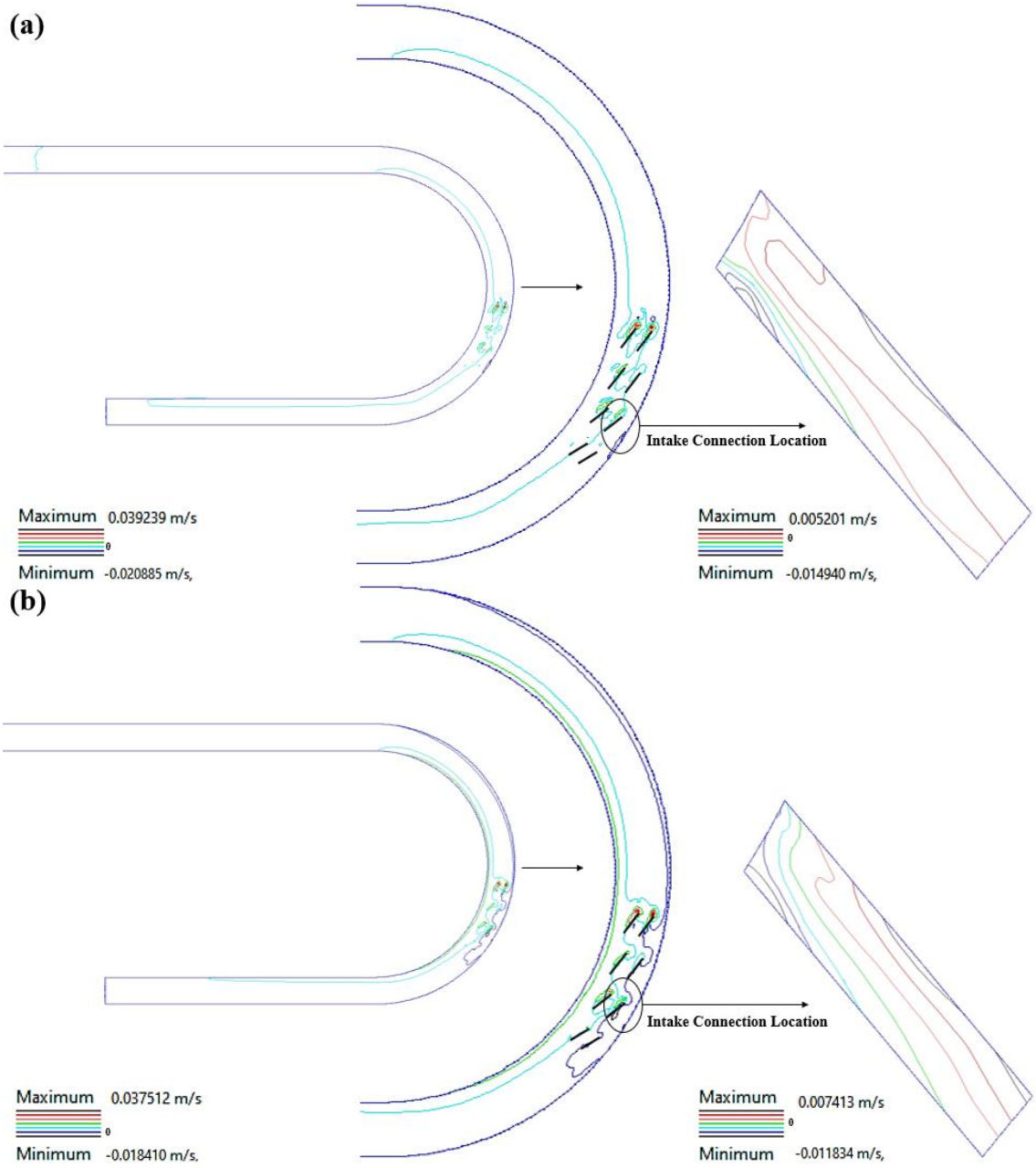
A comparison of streamwise velocities at five levels in the main channel, as shown in Figure 2, revealed that the minimum velocities occurred on the side opposite the vane-induced (inner wall bend). These velocities increased from the bed toward the water surface, likely due to the presence of the submerged vanes and the effect of bed friction.

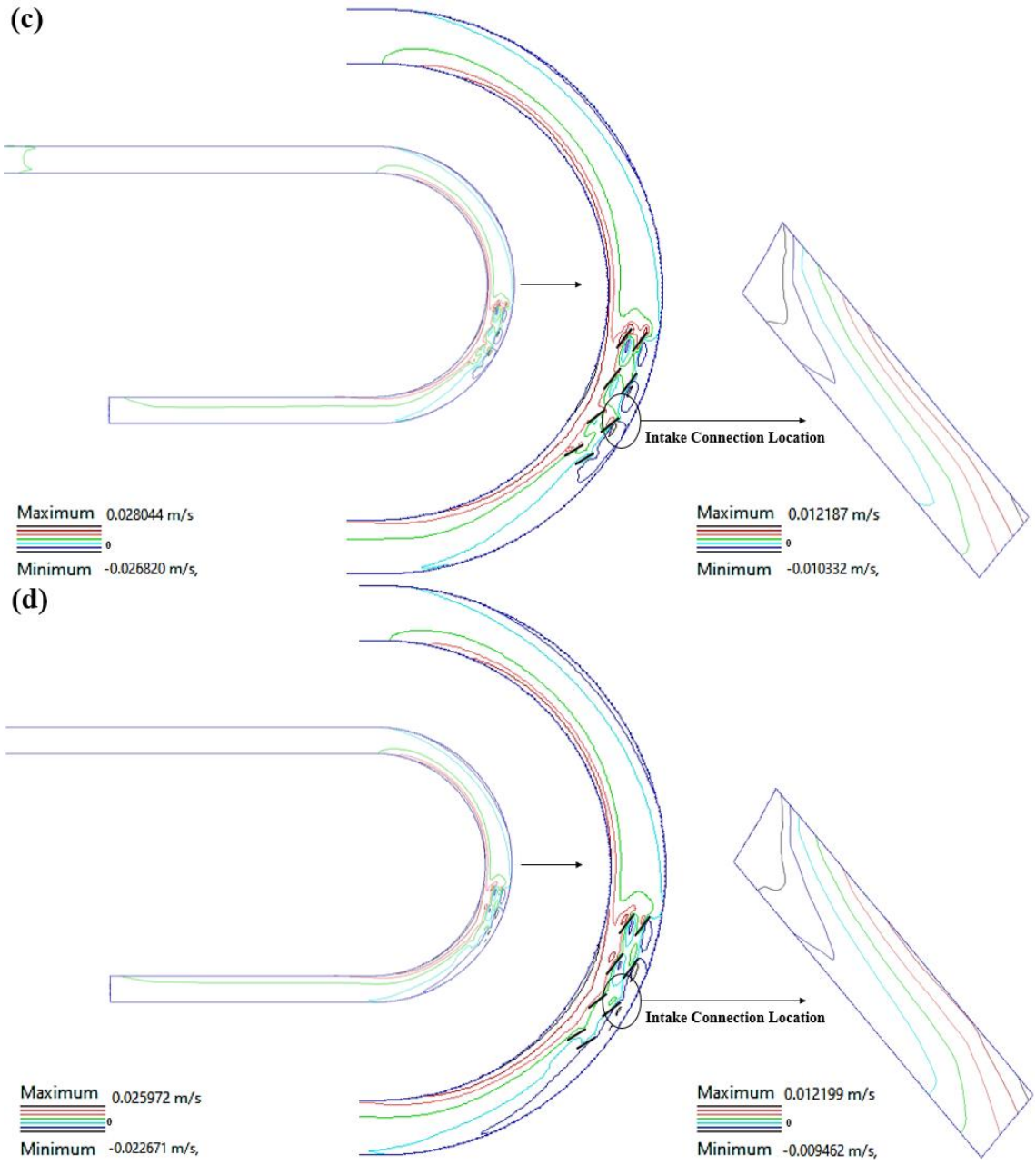
Analysis of maximum streamwise velocities at different levels showed an initial increase from the bed up to $h/y = 0.8$, then decreased toward the water surface. The highest streamwise velocities were observed near the outer bend of the main channel, just downstream of the first row of four paired submerged vanes and in front of the intake. However, the minimum velocities occurred near the inner bend of the main channel, after the end of the intake.

Notably, near-bed maximum velocity cores tended toward the outer bend and intake, while at upper levels, these cores became more dispersed. From the beginning of the channel bend, the trend of increasing velocity with depth was evident; the minimum streamwise velocity decreased, and the maximum streamwise velocity increased.

Within the intake as flow entering the water intake, streamwise velocity patterns showed that, as the flow moved from the bed to the surface, minimum velocities decreased while maximum velocities increased. The highest velocities were recorded at the intake entrance and along the right wall, whereas the lowest velocities occurred along the left wall of the intake.

As shown in Figure 3a, the maximum vertical velocity cores occurred near the first pair of vanes, with the higher values occurring near the vanes. Moving away from this region—both laterally and longitudinally—the vertical velocities decrease.


(a)
Intake Connection Location
Maximum 0.039239 m/s
0
Minimum -0.020885 m/s,
Maximum 0.005201 m/s
0
Minimum -0.014940 m/s,
(b)
Intake Connection Location
Maximum 0.037512 m/s
0
Minimum -0.018410 m/s.
Maximum 0.007413 m/s
0
Minimum -0.011834 m/s,


(c)
Intake Connection Location
Maximum 0.028044 m/s
0
Minimum -0.026820 m/s,
Maximum 0.012187 m/s
0
Minimum -0.010332 m/s,
(d)
Intake Connection Location
Maximum 0.025972 m/s
0
Minimum -0.022671 m/s,
Maximum 0.012199 m/s
0
Minimum -0.009462 m/s,

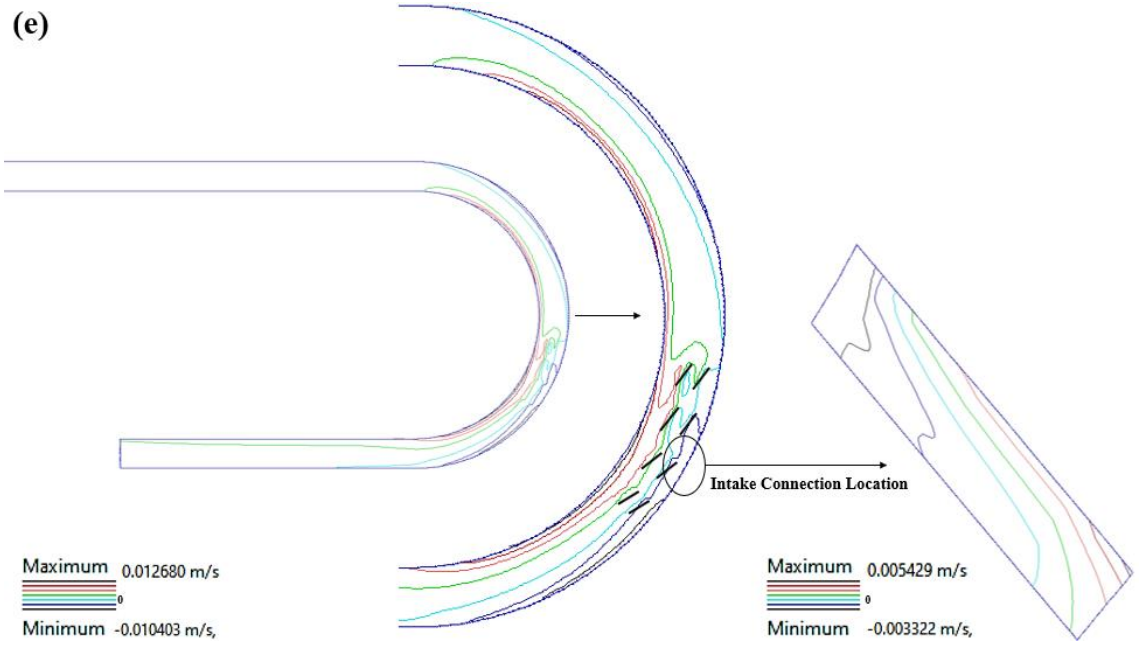


Figure 3. Vertical velocities in main channel and intake (Vane Height is 6cm) a) h/y=0, b) h/y=0.3, c) h/y=0.6, d) h/y=0.8, e) h/y=0.975

After the flow passed the first pair of vanes, the vertical velocity contour lines around the other vane pairs showed lower velocities compared to those near the initial vanes. At higher levels above the bed, the maximum vertical velocity cores shifted toward the inner bend, even though they initially occurred near the first vane pair. Notably, at the last measured depth (Figure 3e), the maximum velocity core moved toward the inner bend, and the influence of the vanes became negligible.

As seen in Figures 3a and 3b, negative vertical velocities occurred near the initial pair of vanes and extended widely across the channel width. In contrast, above the submerged vanes (Figures 3c and 3d), negative velocity cores appeared near the outer bend, particularly in the vicinity of the first row of vanes. This pattern indicates the presence of localized pressure gradients and vertical flow directed toward the bed, resembling scour-inducing conditions observed around bridge foundations [60]. Closer to the water surface, although negative vertical velocities were still observed near the outer bend, their cover extent diminished, and the velocity contours also became more parallel. This observation indicates a decreased influence of the submerged vanes. The variation in minimum vertical velocity from the bed of the main channel to the water surface showed an oscillatory trend. In such a way that initially, the absolute value of the vertical velocity decreased up to h/y = 0.3, then increased at h/y = 0.6, and finally decreased again as it approached the water surface. The highest concentration and gradient of velocity contour lines were observed at the same level of h/y = 0.6.

Maximum positive vertical velocities were detected near the first pair of vanes and at the inner bend of the channel, indicating an upward flow direction toward the water surface in these regions.

Negative vertical velocities were observed at the intake inlet, with their absolute values decreasing as the flow moved away from the bed. At all levels, velocity contours representing negative values extended across much of the intake area, shifting toward the right wall. The maximum positive vertical velocities increased with increasing levels from the bed up to h/y = 0.8, after which they decreased as the flow neared the water surface. The overall maximum absolute

vertical velocity in the main channel occurred near the bed, where negative velocity values indicated a downward flow.

3.3.2 Vane optimal length

For the optimal vane length, considerable stream-wise velocity gradients were observed near the submerged vanes and at the intake inlet (Figure App.1 in the appendix). Moving away from the bed, the concentration of average velocity cores formed around the submerged vanes, indicating their continued influence on the flow field. Even beyond the footprint of the vanes, their impact persisted, as evidenced by the presence of distinct velocity cores above them. However, this influence diminished at h/y = 0.975, where the velocity contours became nearly parallel and the lower velocity values were observed near the inner bend.

It is also noteworthy that the concentration of maximum velocity cores consistently tended toward the outer bend wall. As the flow approached the water surface, these cores extended toward the upstream section of the bend, indicating a wider dispersion of high-velocity regions in the upper flow layers.

Additionally, a comparison across different levels revealed that, as the distance from the bed increased, the minimum stream-wise velocity in the main channel also increased, while it decreased within the intake. The lowest stream-wise velocities were observed along the inner bend of the main channel and near the left wall of the intake. In contrast, the highest stream-wise velocities in the main channel occurred along the outer bend, just downstream of the first pair of submerged vanes. Within the intake, the maximum velocities originated near the left corner of the inlet and extended toward the central axis and right wall. Furthermore, the results indicated that reducing the vane length from 18 cm to 15 cm led to a general decrease in stream-wise velocity in both the main channel—particularly in the region influenced by the submerged vanes—and the intake.

Analysis of the vertical velocity contours illustrates that near the bed, maximum vertical velocity cores formed around the submerged vanes and extended toward the inner bend (Figure App.2 in the appendix). From the bed up to y/h = 0.6, strong velocity cores remained visible around the first pair of vanes, while velocities around the subsequent vane pairs gradually decreased. lose to the bed, the minimum vertical velocities—characterized by negative values—were concentrated near the outer bend and in a small area behind the first pair of vanes. Moving away from the bed to y/h = 0.3, the extent of negative velocity regions expanded, still concentrated near the outer bend and behind the first pair of vanes. At this level, the negative vertical velocities covered a larger section of the main channel width, including areas behind all the vane rows and near the outer bend, indicating a notable downward flow up to the vane height. Beyond the height of the submerged vanes, the influence of the vanes diminished, and the negative velocity cores became smaller, primarily near the outer bend and downstream of the vanes. As the flow passed the lateral intake and exited from the bend, the vertical velocity contours became more uniform and parallel, with maximum positive velocities observed near the inner bend and minimum (negative) velocities persisting near the outer bend.

A comparison of the vertical velocity contours within the intake at different levels revealed that, near the bed, maximum vertical velocities originated from the left corner of the intake inlet and aligned parallel to the intake wall as the flow progressed. The maximum positive vertical velocities were concentrated near the left wall, while the lowest (negative) velocities were observed along the right wall. Moving away from the bed, the contours representing minimum velocities originating from the left corner and extending diagonally toward the far-right corner of the intake. As the vane length decreased from 18 cm to 15.6 cm, negative vertical

velocities continued to appear in the regions influenced by the submerged vanes, near the outer bend of the main channel, and at the intake inlet. In the main channel, the variation in absolute negative vertical velocities from the bed to the water surface exhibited an oscillatory pattern, whereas in the intake, this trend showed a consistent decrease. Similarly, the maximum vertical velocity in the main channel followed an oscillatory trend with depth, mirroring the behavior of the absolute minimum values. In contrast, within the intake, the maximum vertical velocity increased up to y/h = 0.6 and then decreased as the flow approached the water surface.

3.3.3 Vane optimal transverse distance

Stream-wise velocities in different levels revealed that the maximum velocities occurred near the outer bend, with the highest concentrations found close to the bed, particularly around the submerged vanes and the intake (Fig. App.3 in the appendix). As the flow approached the water surface, these high-velocity regions expanded and extended upstream toward the beginning of the bend. In contrast, the minimum velocities were observed along the inner bend wall, gradually shifting toward the water surface and extending downstream after passing the intake, eventually covering the entire width of the main channel. The velocity contours indicated that the maximum velocity core was concentrated around the first pair of submerged vanes, on the side opposite the flow direction. As the flow continued past the subsequent vane pairs, the streamwise velocities decreased. Moving upward from the bed, the velocities around and downstream of the vanes declined, showing strong velocity gradients. Further along the channel, stream-wise velocities continued to decrease, and the velocity contours tended toward the inner bend. Near the water surface, the velocity gradients became weaker, and at the highest depth level, the velocity cores associated with the submerged vanes and intake disappeared—indicating the diminishing effect of the submerged vanes. The results also indicated that the highest stream-wise velocities within the intake, near the bed, originated from the left corner of the intake and developed parallel to the intake wall as the flow progressed. Maximum vertical velocities were observed along the right wall of the intake, while minimum velocities occurred near the left wall. This pattern persisted with increasing height from the bed, where the minimum velocities consistently appeared near the left wall and the maximum velocities near the right wall.

Overall, it can be concluded that decreasing the transverse spacing between the submerged vanes led to a reduction of the maximum streamwise velocity. Furthermore, the results revealed that the highest stream-wise velocities occurred not only at the outer bend of the main channel and the intake inlet but also in the region between the first two pairs of vanes facing the flow. In the main channel, both minimum and maximum velocities generally increased with height. However, while the maximum stream-wise velocity increased up to the level of y/h = 0.8, it declined beyond this point toward the water surface. In contrast, the minimum velocity continued to increase throughout the vertical profile. Analysis of the vertical velocity contour lines revealed that the maximum vertical velocity cores formed near the bed around the second pair of submerged vanes facing the flow. As the distance from the vanes increased, vertical velocities progressively decreased (Fig. App.4 in the appendix). However, as the distance from the bed increased, velocity gradients intensified. Minimum velocity cores developed on the left side of the vanes, while maximum velocity cores formed on the right, extending toward the outer and inner bend walls, respectively. Notably, even in regions without submerged vanes, their influence persisted, as evidenced by the continued presence of velocity cores. At y/h = 0.975, although prominent velocity gradients remained

around the submerged vanes and the intake, the velocity cores appeared more localized. In this layer, the maximum vertical velocities tended toward the inner bend wall, while the minimum velocities moved toward the outer bend wall. Within the intake, the vertical velocity gradients consistently decreased from the bed to the water surface, with maximum velocities observed near the left wall and minimum velocities concentrated near the right wall.

Overall, the results indicated that positive vertical velocities near the bed and around the submerged vanes were higher than at other depth levels within the main channel. The minimum vertical velocities, which were negative, were observed at various levels—near the bed at the downstream end of the submerged vane region, and near the water surface beyond the zone influenced by the vanes. In the intake, the maximum vertical velocity occurred near the left wall at a depth corresponding to y/h = 0.6, which is approximately above the height of the submerged vanes. In contrast, the minimum vertical velocities—also negative—were present across the entire width of the intake at all evaluated levels. As the flow progressed, these negative velocity regions expanded laterally toward the right wall of the intake. Near the bed, the area covered by negative velocities was relatively limited, but this area increased with elevation, occupying a larger portion of the flow field at higher levels.

3.3.4 Vane optimal longitude distance

Compared to the previous sections, the results for the optimal longitudinal spacing of the vanes show that reduced spacing led to greater concentration and density of stream-wise velocity contours. The maximum velocity cores were observed near the outer bend wall, within the region influenced by the submerged vanes and the intake (Fig. App.5 in the appendix). Around the submerged vanes, velocities decreased, and as the flow moved toward the inner bend wall, a continued reduction in velocity was observed. With increasing distance from the bed, the maximum velocity cores expanded upstream, toward the entrance of the bend and the approaching straight channel. Up to y/h = 0.8, the presence of significant velocity gradients indicated that the influence of the submerged vanes remained pronounced. However, by y/h = 0.975, this effect had nearly dissipated, and the velocity contours became nearly parallel, reflecting a diminished impact of the vanes. At the intake inlet, the maximum stream-wise velocities covered the entire width of the intake, with the highest velocity contours gradually tending toward the right wall. As the flow progressed along the intake, the minimum velocity contours appeared near the left wall and persisted to the end of the intake—this pattern was consistent across all levels. In the main channel, the minimum stream-wise velocity showed an increasing trend from the bed toward the water surface. In contrast, in the intake, an oscillatory pattern is exhibited in its minimum velocity distribution with depth. Similarly, the maximum stream-wise velocity in the main channel followed an oscillatory trend with increasing depth, whereas in the intake, it increased steadily as the flow approached the water surface.

The results indicated that for the vane's optimal longitudinal spacing, the maximum vertical velocity cores formed around the vanes from near the bed up to the top of the vane height, particularly near the vanes located adjacent to the inner bend wall (Fig. App.6 in the appendix). Moving laterally away from the vanes toward the outer bend wall, vertical velocities gradually decreased. Similarly, near the bed, velocities also declined when moving toward the inner bend wall. However, at the depth of y/h = *0.3*, the region of maximum vertical velocities expanded toward the inner bend. In this region, the area occupied by negative vertical velocities also widened, covering a larger portion of the main channel width. As the distance from the bed increased, the velocity cores continued to reflect the influence of the submerged vanes, although the vertical velocity gradients became

weaker closer to the water surface. At the upper three depth levels, the maximum velocity cores tended toward the inner bend wall, while the minimum (negative) velocity cores were concentrated near the outer bend wall. A comparison of vertical velocity contours at different depth levels revealed that, at the intake inlet, the minimum vertical velocities initially covered the entire width of the intake. As the flow progressed, these low-velocity regions expanded and occupied a larger portion of the flow field. Conversely, the maximum vertical velocities were concentrated near the left wall of the intake and gradually extended toward its downstream end. In the main channel, both the maximum vertical velocity and the absolute minimum vertical velocity (the latter being negative) displayed oscillatory trends with increasing depth. In contrast, the absolute minimum vertical velocity within the intake decreased consistently from the bed to the water surface. Meanwhile, the maximum vertical velocity in the intake also exhibited an oscillatory pattern, similar to that observed in the main channel.

3.3.5 Optimal distance of the first row from the intake

As previously noted, the maximum stream-wise velocity contours were concentrated near the outer bend wall (Fig. App.7 in the appendix). The results further indicated that these maximum velocities extended not only along the outer bend but also into the region between the submerged vanes. In contrast, lower velocities were observed around the vanes. As the flow progressed, low-velocity cores developed around the vanes and gradually tended toward the inner bend wall. With increasing distance from the bed, the general trend remained: maximum velocities were concentrated near the outer bend wall, while minimum velocities were directed toward the inner bend wall. However, the stream-wise velocity gradients decreased with height.

At the intake inlet, the highest stream-wise velocities initially occupied the entire width of the intake but progressively tended toward the right wall as the flow moved downstream. Meanwhile, the minimum stream-wise velocities were observed near the left wall, farther from the intake entrance. A comparison of the maximum velocities at various distances from the bed in the main channel revealed an increasing trend up to $y/h = 0.6$, followed by a gradual decrease toward the water surface. This decrease occurred with significantly smaller gradients compared to the lower levels. In contrast, the minimum velocity decreased up to $y/h = 0.3$ and then increased toward the water surface. In the intake, the maximum stream-wise velocity consistently increased with height. However, the minimum velocities showed an oscillatory pattern—initially decreasing, then increasing, and finally decreasing again as the flow approached the water surface.

The analysis of vertical velocity contour lines showed that the maximum vertical velocity cores were concentrated around the submerged vanes at the three levels closest to the bed. As the distance from the bed increased, the velocity gradients around the vanes decreased (Fig. App.8 in the appendix). Closer to the water surface, with decreasing velocity gradients in the region influenced by the submerged vanes, the area occupied by the maximum velocities expanded laterally and tended toward the inner bend wall, consistent with observations from previous sections. The minimum velocity contours were consistently located near the outer bend wall at all examined levels. At the intake inlet, the minimum velocities covered the entire width of the intake at all levels. As the distance from the bed increased, these minimum velocities occupied a larger portion of the intake cross-section and tended toward the right wall. Conversely, the maximum velocities consistently appeared farther downstream from the intake inlet, near the left wall, and extended toward the end of the intake. The negative values of the minimum vertical velocities in both the main channel and the intake indicate the presence of downward flow. In

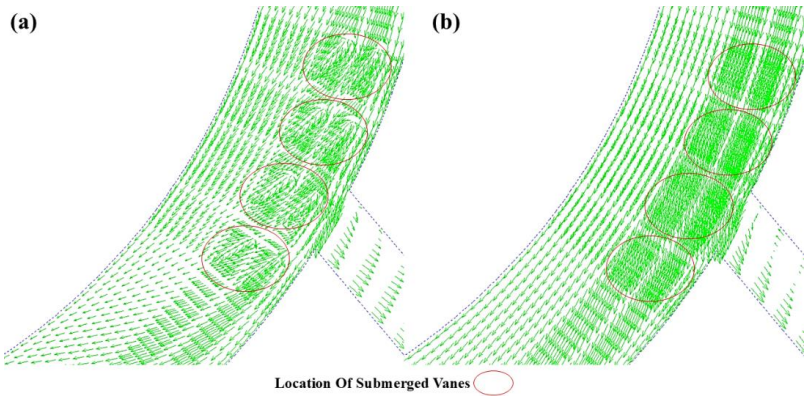


Figure 4. Streamlines at (a) the bed and (b) the water surface.

the main channel, these negative velocities were concentrated near the outer bend and, at levels y/h = 0.3 and 0.6, covered a significant portion of the channel width. However, closer to the water surface, the extent of the area affected by negative velocities decreased. At the intake inlet, all vertical velocities were negative. As the flow progressed, negative velocity contours tended toward the right wall, while positive velocities developed near the left wall. The analysis also revealed that with increasing distance from the bed, a larger portion of the intake became dominated by negative vertical velocities. In the main channel, the absolute minimum vertical velocity increased with height up to y/h = 0.8, beyond which it began to decrease toward the water surface. Similarly, in the intake, the absolute minimum vertical velocity increased up to y/h = 0.6, followed by a gradual decrease near the surface. Notably, the trends in maximum vertical velocity differed between the intake and the main channel. In the intake, the maximum vertical velocity increased with height up to y/h = 0.8 and then decreased toward the water surface. In contrast, the maximum vertical velocity in the main channel exhibited an oscillatory pattern throughout the flow depth.

3.4 Vorticity and Secondary Flow

When the water flows in a channel with the aspect ratio of less than 5, or when the flow path is curved—causing centrifugal forces to become dominant—secondary flows are typically intensified. Additionally, the presence of submerged vanes on the bed of the main channel further enhances these secondary and vortex flows, significantly influencing the overall flow structure [61, 62, and 63]. On the other hand, installation of submerged vanes caused modification in formed secondary flows from the outer wall to the inner wall, near the bed. This modification caused a reduction in the strength of secondary currents and reduced bank erosion [64]

Figure 4 illustrates the streamlines interacting with the submerged vanes and their deflection toward the intake at two levels: the channel bed and the water surface. As evident from the figure, the combined influence of the submerged vanes, channel bend, and intake generates strong eddy currents.

Given the significance of the vortices formed within the flow, vorticity contour lines are presented in Figure 5 to quantitatively illustrate this flow parameter. In the figure, the direction of flow is oriented downward.

In Figure 5, the stream-wise vorticity is defined as:

$$Vor = \frac{\partial w}{\partial r} - \frac{\partial u}{\partial z} \tag{8}$$

The channel with a 180° bend is shown for the simulation run.

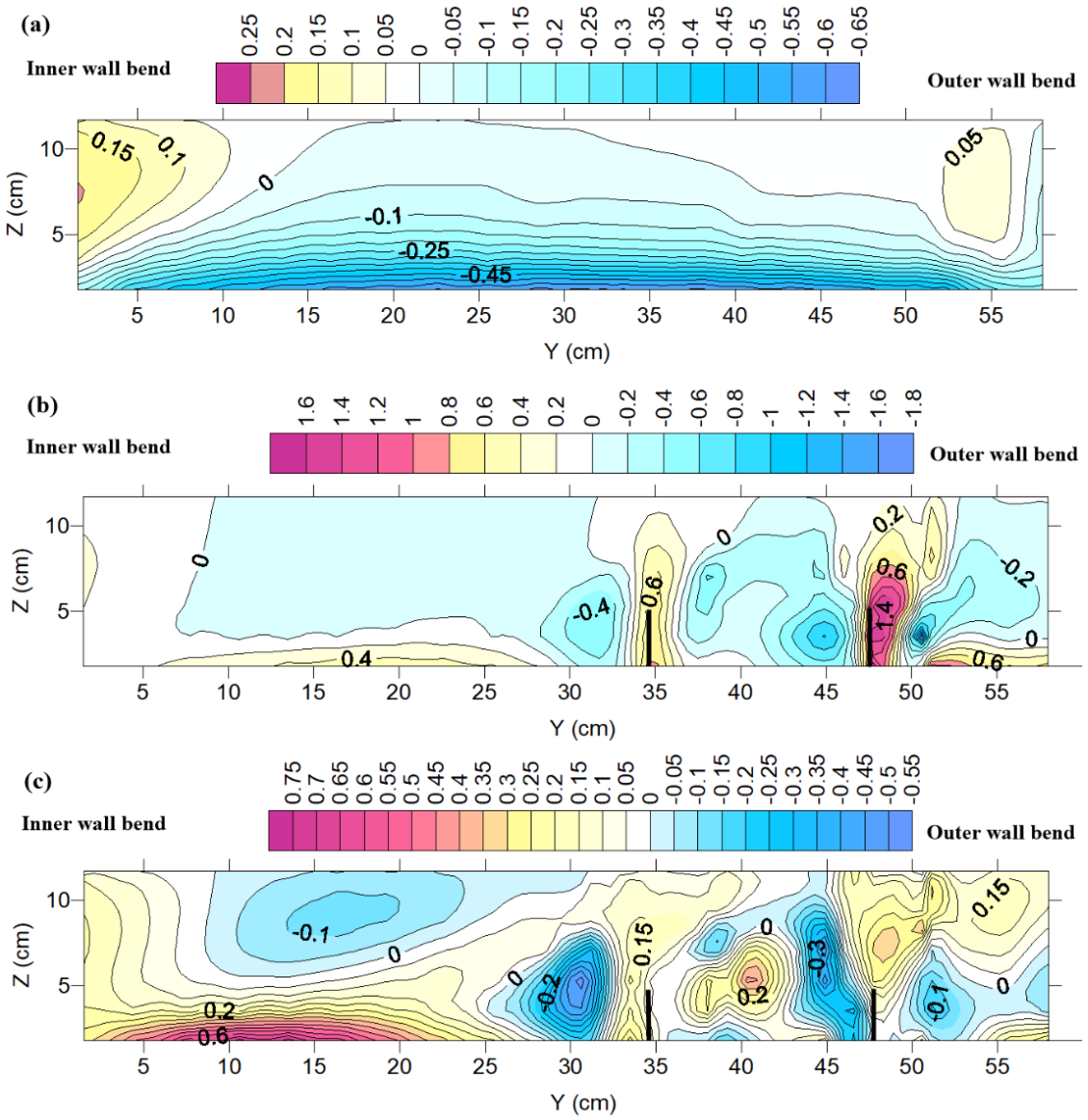


Figure 5. Vorticity in three cross-sections a) in the middle of the curvature of the bend, b) in front of the water intake, and c) after the water intake in line with the last pair of submerged vanes

Vorticity contour lines were analyzed at three cross-sections: in the middle of the bend, in front of the water intake, and downstream of the intake near the last pair of submerged vanes. As shown in Figure 5a, in the middle of the 180-degree bend, two positive vorticity cores appear near the inner and outer walls. Vorticity values decrease toward the center of the main channel width. The presence of negative vorticity in the middle of the channel and near the bed suggests stronger longitudinal velocity gradients compared to vertical velocity gradients. The contour lines are mostly parallel, with steeper gradients observed near the channel bed.

In contrast, the vorticity distribution at the cross-section aligned with the midpoint of the intake reveals a different pattern due to the influence of the submerged vanes (Fig. 5 b). In this figure, the submerged vanes are represented by two bold black vertical lines. Positive vorticity cores are clearly concentrated around the vanes, with the highest vorticity occurring near the vane closest to the intake. Since turbulence

intensity is derived from velocity fluctuations, and vorticity also arises from changes and fluctuations in velocity; it discussed that there is a relationship between turbulence intensity and vorticity and turbulence intensity increased near the intake inlet. This indicates strong vertical velocity gradients and intensified secondary flow in the vicinity of the vanes as showed in Figure 3a previously. Elsewhere in the flow field, negative vorticity dominates, suggesting that longitudinal velocity gradients exceed vertical gradients. Additionally, positive vorticity values are observed near the bed and are inclined toward the inner bend.

As previously noted, the final cross-section was selected downstream of the intake, aligned with the midpoint of the last pair of submerged vanes (Fig. 5c). The contour lines in this section indicate that the maximum vorticity occurred near the bed and tended toward the inner wall of the bend. In addition, positive vorticity values were present in the region between the two vanes and in the upper flow layers above the vane closest to the intake, reaching toward the outer bend wall. Negative vorticity cores appeared on the right side of both vanes (moving in the direction of the flow), reflecting the dominance of longitudinal velocity gradients over vertical ones in those regions. Observation of Figures 5b and 5c clearly highlights the role of the presence of the water intake. The presence of the intake induced strong secondary flows and concentrated positive vorticity near the bed in the cross-section aligned with the center of the intake. However, downstream of the intake, these intensified flow patterns shifted upward, with strong currents observed closer to the water surface.

From another perspective, spiral flows induced by centrifugal forces in a curved channel are another clear manifestation of secondary flow development [65]. The strength of these secondary flows can be quantified using the following equation:

$$V_s = V_i - V_{i-1} \quad (9)$$

Where V_i is the transverse velocity component at the upper layer of the water column, and V_{i-1} is the transverse velocity component at the adjacent lower layer. The index i corresponds to the vertical discretization levels used in the depth-wise mesh. Figure 6 illustrates the variations in the dimensionless secondary flow strength (Vs/V), where V is the average transverse velocity component in the main channel, across three different cross-sections.

As shown in Figure 6, at the first cross-section—located in the middle of the bend—the secondary flow strength was greatest near the bed and gradually decreased with depth, reaching a minimum value of -0.05 at the water surface.

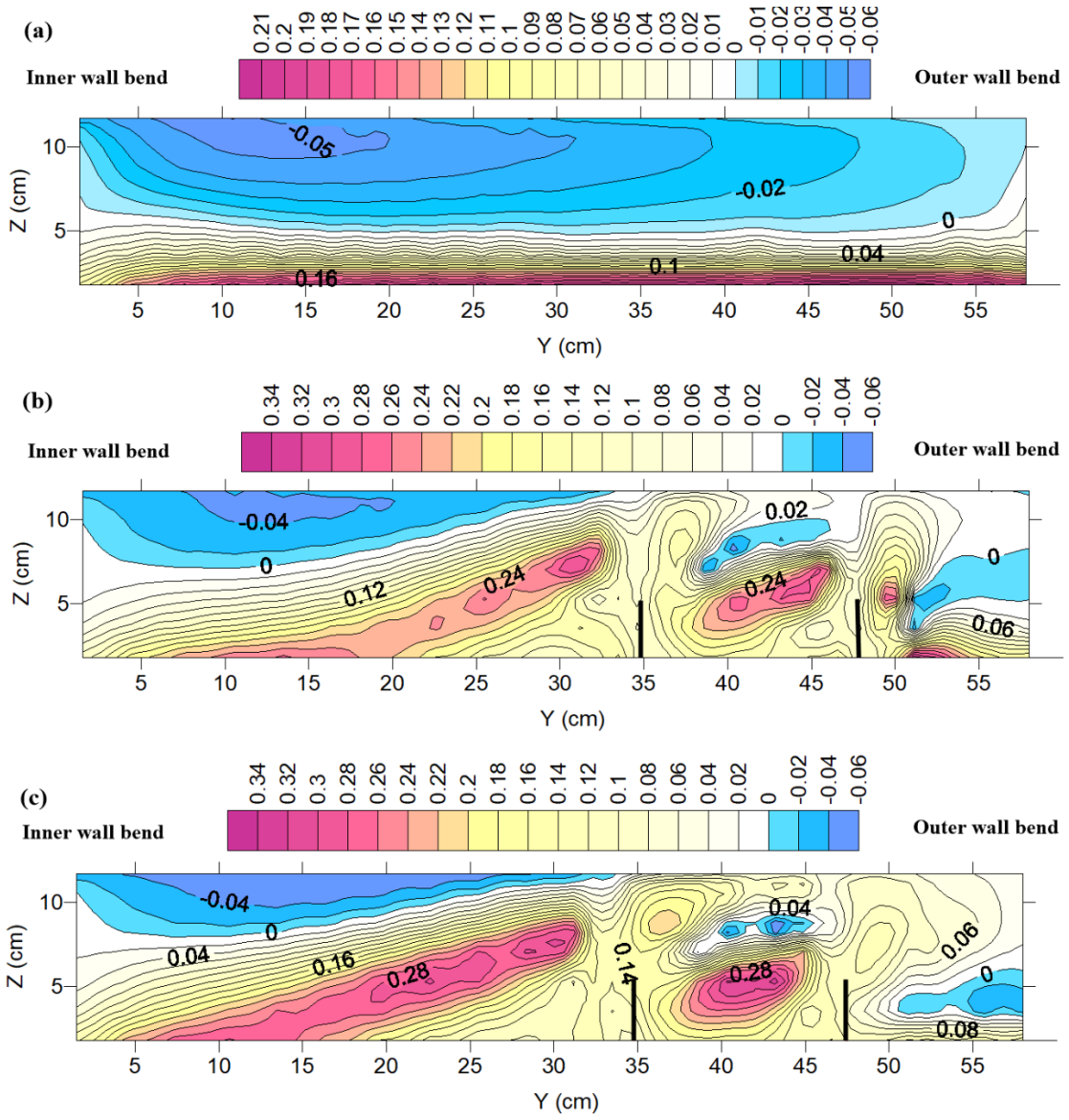


Figure 6. dimensionless strength of the secondary flow for three cross-sections a) in the middle of the curvature of the bend, b) in front of the water intake, and c) after the water intake in line with the last pair of submerged vanes

Additionally, a comparison of secondary flow strength between the inner and outer walls of the bend reveals that, although the difference was small, the strength was slightly higher along the outer wall. In the second cross-section, located opposite the midpoint of the intake, the presence of submerged vanes and the intake itself significantly influenced the formation of secondary flow strength contours. In this section, the cores of maximum secondary flow strength were observed on the right side of the submerged vanes (assuming flow direction is used as the reference). The results also indicated that the positive secondary flow strength values above both vanes extended all the way to the water surface. Unlike the previous section, no negative values of secondary flow strength were present at the surface. Furthermore, the maximum strength of secondary flow in this cross-section was greater than that in the previous one. At the intake inlet, the highest secondary flow strength occurred

near the bed, with positive values observed both near the bed and at the water surface, while negative values appeared in the mid-depth region. This distribution clearly reflects the presence of vortex and spiral flow structures. In the third cross-section—located downstream of the intake within the main channel—the pattern of secondary flow strength, including its minimum and maximum magnitudes around and above the submerged vanes toward the water surface, was generally similar to that observed in the second section. However, at the intake inlet, although the overall pattern remained consistent with the second section, the maximum value of the secondary flow strength was decreased, and the core of negative flow strength values was positioned closer to the channel bed.

4. Conclusion:

This study investigated the flow structure of sediment-water in an experimental channel with a 180-degree bend and a lateral intake positioned at a 120-degree angle. To reduce sediment entry into the lateral intake, two rows of submerged vanes (each consisting of four vanes) were installed at a 45-degree angle relative to the main channel flow direction. The optimal computational mesh size was evaluated to be 2.7 × 1 units in the flow and channel width directions, respectively, yielding a sediment transport estimation error of only 0.55%. Results indicated that the optimal vane height and length were 6 cm and 15 cm, respectively—corresponding to 0.5 times the flow depth and 2.5 times the vane height. Furthermore, the optimal transverse and longitudinal spacings between the vanes were 2.17 and 5 times the vane height, while the distance from the closest vane row to the intake was twice the vane height.

A comparison of this study's results with previous research reveals that Ouyang [32] identified the optimal vane height as ranging from 0.58 to 0.7 times the flow depth. The present study's result (H/y = 0.5) are in complete agreement with the presented range, but remains closely aligned with values reported by Odgaard and Wang [27]. Conversely, Tan et al. [31] reported a smaller optimal height range of 0.125 to 0.33 times the flow depth, which differs significantly from the findings of this study. Additionally, Tan et al. [31] investigated vane length and found the optimal range to be 2.5 to 10 times the flow depth, whereas the current study determined a ratio of 1.25. A key factor contributing to the discrepancy may be that Tan et al. [31] accounted for bed form development in their analysis, which can significantly influence flow structure, depth, and sediment transport.

Although international studies have not extensively investigated the effects of varying the longitudinal and transverse spacing between submerged vanes, or their distance from the intake, local research provides some insights. Davoudi and Shafai [66] found that the optimal longitudinal spacing between vanes was eight times the vane height. Similarly, Montasseri et al. [67] reported that the optimal distance from the first row of vanes to the outer wall of the bend was two times the vane height, while the optimal transverse spacing between vanes was 1.5 times the vane height.

Kalathil et al. [51] reported that the use of collars and submerged vanes reduced sediment ingress into lateral channels by 46.82% and 85.36% at vane angles of 15° and 40°, respectively. Moradinejad et al. [7] demonstrated that combining skimming walls with spur dikes enhanced sediment reduction efficiency at intakes, achieving up to 81% effectiveness. Farshidnia et al. [3] found that optimizing the length and height of parallel skimming walls significantly improved sediment control at lateral intakes, with sediment reduction efficiencies reaching up to 74%. Fahmy et al. [68] employed baffle columns as an alternative to avoided walls, achieving a 71% reduction in accumulated sediment within the intake. Ezz-Aldeen et al. [69] investigated sedimentation at a pumping station in the Mosul Dam reservoir through simulations. Their results showed that using a combination of dykes and strategic

placement reduced sediment deposition within the intake and pumping station by 42%. Despite variations in the experimental conditions across different studies, the reported reductions in sediment inflow to intake using different countermeasure structures were generally consistent with the findings of the present study. Here, by optimizing key design parameters, sediment inflow to the intake was reduced by up to 63%.

Analysis of the flow structure across all scenarios with optimal parameters revealed that near the bed, the cores of maximum stream-wise velocity were directed toward the outer bend and the intake. As the flow approached the water surface, these high-velocity cores expanded and became evident from the onset of the bend. The minimum vertical velocities (negative values) were concentrated at the intake inlet and decreased with increasing distance from the bed. At all depth levels within the intake, negative velocity streamlines covered a significant portion of the intake cross-section and tended toward the right wall. The findings also indicated that the highest stream-wise velocities in the intake occurred near the right wall, whereas the maximum vertical velocities were concentrated near the left wall. Reducing the vane length from 18 cm to 15 cm led to a decrease in stream-wise velocity both in the main channel—particularly in regions influenced by the submerged vanes—and within the intake. A reduction in the transverse spacing between vanes also resulted in lower maximum streamwise velocities. Karami et al. [34] demonstrated that increasing the longitudinal spacing between consecutive submerged vanes leads to greater velocity gradients—a finding corroborated by the results of the present study. Additionally, while reducing the distance between the submerged vanes and the intake had minimal impact on the velocity distribution at higher elevations above the bed, it generally contributed to a reduction in streamwise velocity throughout the flow field.

This study also examined the presence and intensity of secondary currents. In the absence of submerged vanes, the maximum secondary current strength was concentrated near the bed and extended across the entire width of the main channel. However, the introduction of submerged vanes altered the distribution pattern of secondary current strength. With the vanes in place, the cores of maximum secondary current strength shifted to the left side of the vanes, and the region exhibiting negative current strength near the intake showed a noticeable reduction in surface area. This research's findings provide engineers and designers with valuable guidance for the effective implementation of submerged vanes, enabling a substantial reduction in sediment ingress. This improvement not only lowers operational and maintenance costs but also contributes meaningfully to the sustainable management of water resources. The findings of this research, when combined with economic considerations and analyses, can open new avenues for future studies in river engineering. By identifying the optimal dimensions and installation spacing of submerged vanes, these results can support more effective implementation in river management and planning projects.

Statements and Declarations

Data availability

All data are available on request.

Funding

This research received no external funding.

Conflict of interest

The authors declare that they have no conflict of interest.

Artificial intelligence (AI) usage

During the preparation of this work, the author(s) used [ChatGPT] in order to improve text writing. After using this tool/service, the authors reviewed and edited the content as needed and take full responsibility for the content of the publication.

Author contributions

All authors contributed to the study conception and design. Conceptualization: [Author 2, Author 3]; Methodology:

[Author 1]; Formal analysis and investigation: [Author 1, Author 2, Author 3]; Writing - original draft preparation: [Author 2]; Writing - review and editing: [Author 2, Author 1]; Resources: [Author 2, Author 1]; Supervision: [Author 2]

References

1. Fatehi-Nobarian B, Farshidnia S, Saneie M. Effect of hydraulic and geometrical parameters of skimming wall on controlling sediment entering lateral intakes using harmony search algorithm. Advance Researches in Civil Engineering. 2022 Dec 1;4(4):55-70.
2. Moradinejad A, Haghiabi A, Saneie M, Yonesi HA. Investigation of the effect of sediment control structures on the kinetic energy of turbulent in the intake entrance. Irrigation and Drainage Structures Engineering Research. 2021 Apr 21;22(82):121-46.
3. Farshidnia S, Saneie M, Hajikandi H, Rostami M. Experimental investigation of impact of length and height of parallel skimming walls on controlling inlet sediment to lateral intake. Water Supply. 2020 May 1;20(3):997-1005.
4. Farshidnia S, Saneie M, Hajikandi H, Rostami M. Experimental Study on the Placement of the Angle and the Distance of Parallel Skimming Walls to Reduce Inlet Sediment in a Lateral Intake. Slovak Journal of Civil Engineering. 2020;28(2):23-9.
5. Pandey M, Valyrakis M, Qi M, Sharma A, Lodhi AS. Experimental assessment and prediction of temporal scour depth around a spur dike. International Journal of Sediment Research. 2021 Feb 1;36(1):17-28.
6. Zamani M, Rabiefar H, Rostami M. Experimental evaluation of spur dikes placement position effect on the hydraulic and erosion conditions of intakes. Water supply. 2020 May 1;20(3):900-8.
7. Moradinejad A, Saneie M, Ghaderi A, Zamanieh Shahri SM. Experimental study of flow pattern and sediment behavior near the intake structures using the spur dike and skimming wall. Applied Water Science. 2019 Nov;9(8):1-1.
8. Pandey M, Ahmad Z, Sharma PK. Scour around impermeable spur dikes: a review. ISH journal of hydraulic engineering. 2018 Jan 2;24(1):25-44.
9. Firmansyah R, Jauzi MZ, Istiyanto DC, Subarkah A, Sujoko SU, Wibowo M, Yuniardi RC. Study on the design and implementation of BPPT-lock armored groin for sediment control structure in front of sea water intake. Zona Laut Jurnal Inovasi Sains Dan Teknologi Kelautan. 2023 Nov 9:240-7.
10. Fahmy WA, Halawa MA, Hekal NT. Reduction of sedimentation and water turbidity at intakes of drinking water treatment plants. Water Science. 2023 Dec 31;37(1):40-56.
11. Attia K, Elsaid G. The hydraulic performance of oriented spur dike implementation in open channel. InJournal of International Water Technology Conference, IWTC, Alexandria, Egypt 2006 (No. 10, pp. 281-298).
12. Yossef MF. The effect of groynes on rivers. Literature Review. 2002 Aug 23.
13. Haider R, Qiao D, Yan J, Ning D, Pasha GA, Iqbal S. Flow characteristics around permeable spur dike with different staggered pores at varying angles. Arabian Journal for Science and Engineering. 2022 Apr;47(4):5219-36.
14. Moradinejad A, Haghiabi AH, Saneie M, Younesi H. Experimental Study on Sediment Control in a Lateral Intake Channel by Using a Spur Dike Combined with a Skimming Wall. Advances in Civil Engineering and Environmental Science. 2025 May 27;2(2):85-96.
15. Jafari R, Sui J. Velocity field and turbulence structure around spur dikes with different angles of orientation under ice covered flow conditions. Water. 2021 Jul 1;13(13):1844.
16. Veisi F, Jafari A. Three-dimensional Study of Flow Turbulence Extension around Straight, T and L Shaped Groynes in Open Channles using Physical Model. Irrigation

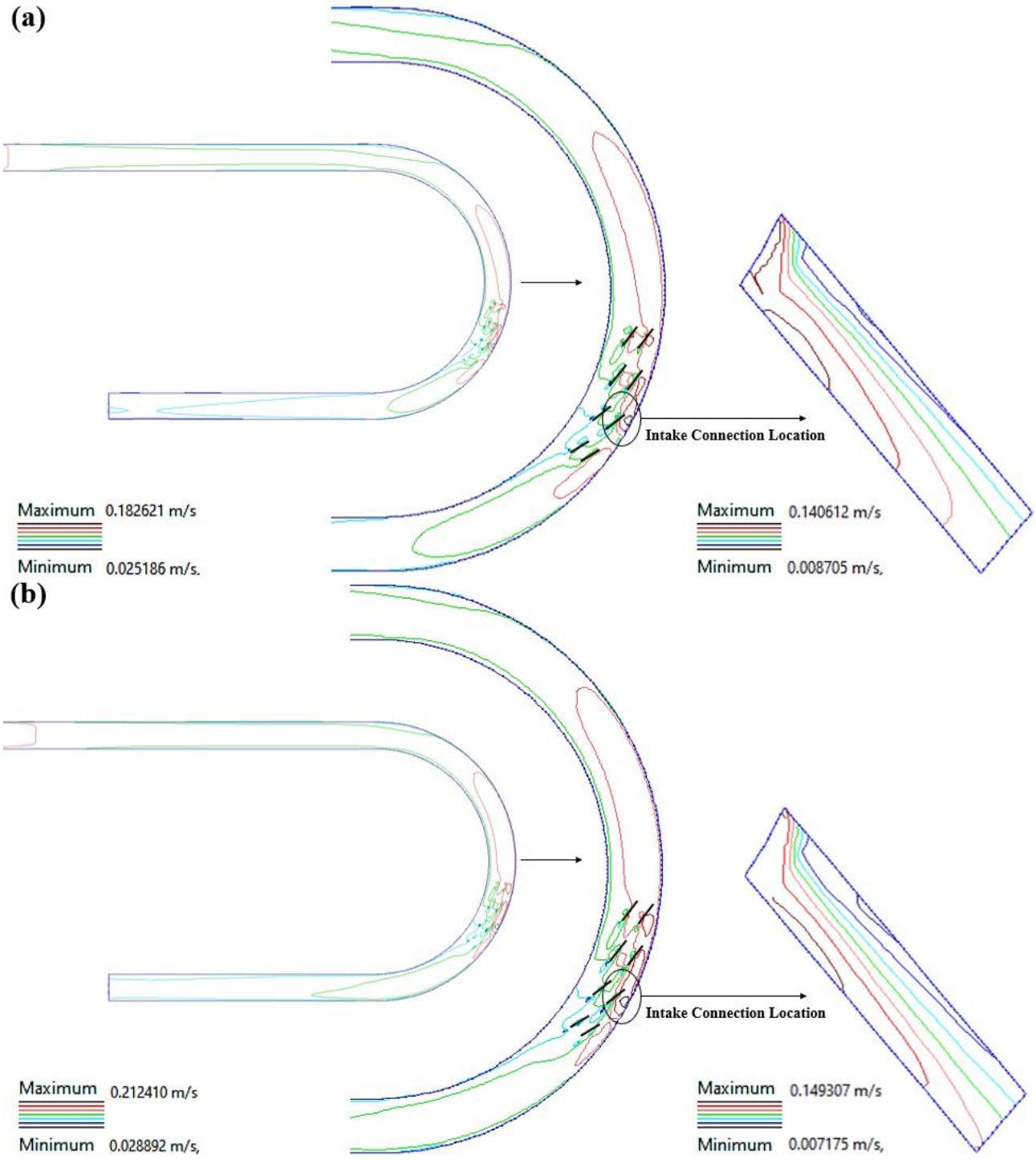
Sciences and Engineering. 2019 Jan 1;42(1):15-29.
17. Kumar L, Afzal MS. Numerical simulations of scour around vertical wall abutments with varying aspect ratios under combined waves and current flows. Journal of Marine Science and Engineering. 2023 Sep 28;11(10):1886.
18. Fathi A, Zarrati AR, Salamatian SA. Scour depth at bridge abutments protected with a guide wall. Canadian Journal of Civil Engineering. 2011 Dec;38(12):1347-54.
19. Vaghefi M, Solati S, Abdi Chooplou C. The effect of upstream T-shaped spur dike on reducing the amount of scouring around downstream bridge pier located at a 180 sharp bend. International journal of river basin management. 2021 Jul 3;19(3):307-18.
20. Hamidi M, Sadeqlu M, Khalili AM. Investigating the design and arrangement of dual submerged vanes as mitigation countermeasure of bridge pier scour depth using a numerical approach. Ocean Engineering. 2024 May 1;299:117270.
21. Dadamahalleh PA, Hamidi M, Khalili AM. Bed sill effect on bridge pier scour with debris obstruction: an experimental investigation. Innovative Infrastructure Solutions. 2024 May;9(5):142.
22. Safaripour N, Vaghefi M, Mahmoudi A. Experimental study of the effect of submergence ratio of double submerged vanes on topography alterations and temporal evaluation of the maximum scour in a 180-degree bend with a bridge pier group. International Journal of River Basin Management. 2022 Oct 2;20(4):427-41.
23. Safaripour N, Vaghefi M, Mahmoudi A. The influence of the submergence ratio of submerged vanes on the slope of the hole around the pier groups in a sharp bend. Journal of Hydraulic Structures. 2024 Apr 1;10(3):90-118.
24. Mahdian Khalili A, Akbari Dadamahalleh P, Hamidi M. Experimental evaluation of dune formation downstream of pier scour hole with upstream debris accumulation. Journal of Hydraulic Structures. 2024 Mar 1;10(1):13-28.
25. Odgaard AJ, Lee HY. Submerged vanes for flow control and bank protection in streams. Iowa City, IA, USA: Iowa Institute of Hydraulic Research, the University of Iowa; 1984 Jul.
26. Odgaard AJ, Mosconi CE. Streambank protection by submerged vanes. Journal of Hydraulic Engineering. 1987 Apr;113(4):520-36.
27. Odgaard AJ, Wang Y. Sediment management with submerged vanes. I: Theory. Journal of Hydraulic Engineering. 1991 Mar;117(3):267-.
28. Barkdoll BD, Hagen BL, Odgaard A. Sediment exclusion at hydropower intakes using submerged vanes. American Society of Civil Engineers, New York, NY (United States); 1995 Dec 31.
29. Marelius F, Sinha SK. Experimental investigation of flow past submerged vanes. Journal of Hydraulic Engineering. 1998 May;124(5):542-5.
30. Gupta UP, Sharma N, Ojha CS. Performance evaluation of tapered vane. Journal of Hydraulic Research. 2007 Jul 1;45(4):472-7.
31. Tan SK, Yu G, Lim SY, Ong MC. Flow structure and sediment motion around submerged vanes in open channel. Journal of waterway, port, coastal, and ocean engineering. 2005 May;131(3):132-6.
32. Ouyang HT. Investigation on the dimensions and shape of a submerged vane for sediment management in alluvial channels. Journal of Hydraulic Engineering. 2009 Mar;135(3):209-17.
33. Sharma H, Jain B, Ahmad Z. Optimization of submerged vane parameters. Sādhanā. 2016 Mar;41:327-36.
34. Karami H, Farzin S, Sadrabadi MT, Moazeni H. Simulation of flow pattern at rectangular lateral intake with different dike and submerged vane scenarios. Water Science and Engineering. 2017 Jul 1;10(3):246-55.
35. Biswas P, Barbhuiya AK. Countermeasure of river bend scour using a combination of submerged vanes and riprap. International Journal of Sediment Research. 2018 Dec 1;33(4):478-92.

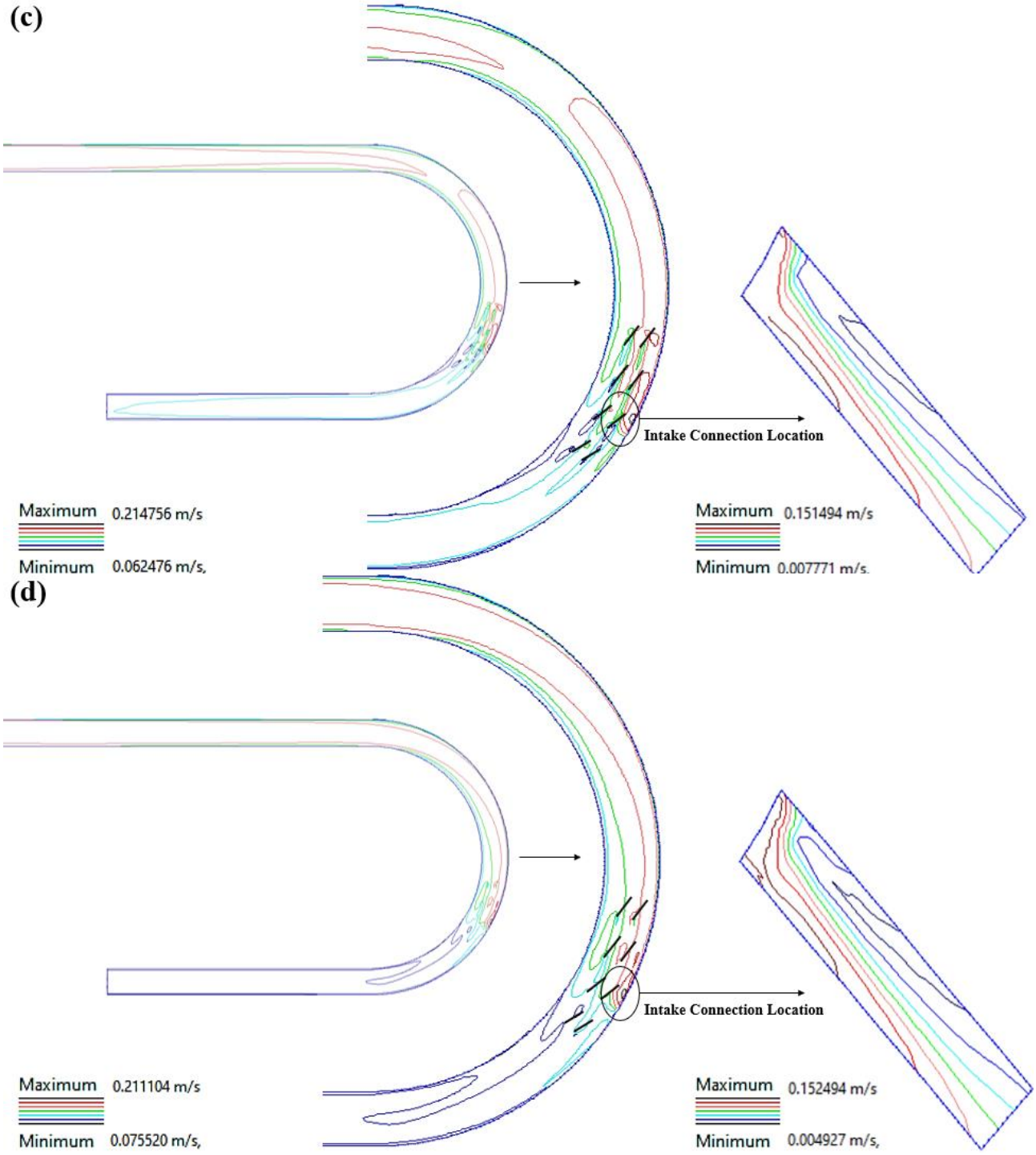
36. Nakato T, Kennedy JF, Bauerly D. Pump-station intake-shoaling control with submerged vanes. Journal of Hydraulic Engineering. 1990 Jan;116(1):119-28.
37. Raudkivi AJ. Sedimentation: exclusion and removal of sediment from diverted water. CRC Press. 1993.
38. Wang Y, Odgaard AJ, Melville BW, Jain SC. Sediment control at water intakes. Journal of Hydraulic Engineering. 1996 Jun;122(6):353-6.
39. Ouyang HT. Design optimization of submerged vane system for sediment control. The University of Iowa; 2001.
40. Ho J, Johnson A, White S. 3-D numerical simulation study of permanent sediment control submerged vanes.
41. Michell F, Ettema R, Muste M. Case study: Sediment control at water intake for large thermal-power station on a small river. Journal of Hydraulic Engineering. 2006 May;132(5):440-9.
42. Sarhadi A, Jabbari E. Investigating effect of different parameters of the submerged vanes on the lateral intake discharge located in the 180 degree bend using the numerical model. Civil Engineering Journal. 2017 Dec 10;3(11):1176-87.
43. Tseng CY, Lee J, Guala M, Musa M. Experimental Tests of Lateral Bedload Transport Induced by a Yawed Submerged Vane Array in Open-Channel Flows. Journal of Hydraulic Engineering. 2024 Nov 1;150(6):04024045.
44. Mhsen MA, Hilo AN. The effects of different lateral channel discharge on one row of submerged vanes. InAIP Conference Proceedings 2023 Dec 22 (Vol. 2977, No. 1). AIP Publishing.
45. Hilo AN. The Effects of submerged vanes inclination angle on sediment transport into sub-channel. Wasit Journal of Engineering Sciences. 2023 Apr 1;11(1):105-15.
46. Aminian P, Jorabloo M, Ahmadi A. Numerical Study of the Effects of Inlet Geometry on the Performance of the Sediment Bypass Tunnel using SSIIM Numerical Model. Journal of Hydraulic and Water Engineering. 2023 Jul 1;1(1):65-75.
47. Chauhan V, Singhal GD, Chavan R. A review of sediment deflection in rivers using submerged vanes. ISH Journal of Hydraulic Engineering. 2023 Aug 8;29(4):514-30.
48. Gumgum F, Cardoso AH. Optimizing the desilting efficiency of submerged vane fields at lateral diversions. Journal of Hydraulic Engineering. 2023 Jan 1;149(1):04022031.
49. Bor A. Experimental investigation of 90 intake flow patterns with and without submerged vanes under sediment feeding conditions. Canadian Journal of Civil Engineering. 2022;49(3):452-63.
50. Baltazar J, Alves E, Bombar G, Cardoso AH. Effect of a submerged vane-field on the flow pattern of a movable bed channel with a 90 lateral diversion. Water. 2021 Mar 18;13(6):828.
51. Kalathil ST, Murugesan MR, Chandra V. Control of sediment entry into intake canals using submerged vanes with collar. InWater Security and Sustainability: Proceedings of Down To Earth 2019 2021 (pp. 209-216). Springer Singapore.
52. Serajian MT, Kamanbedast AA, Masjedi A, Heidarnejad M, Hasonizadeh H. Laboratory evaluation of the combined effect of convergence and submerged vanes on lateral Intakes' sediment input at 90 river bends. Ain Shams Engineering Journal. 2020 Mar 1;11(1):245-52.
53. Karami Moghadam M, Keshavarz A, Sabzevari T. The Effect of Diversion Flow, Intake Inlet Shape, Topography and Bed Roughness on the Flow Separation Dimensions and Shear Stress at the Lateral Intake. Irrigation and Drainage Structures Engineering Research. 2019 Feb 20;19(73):113-26.
54. OLSEN NR. SIMULATION OF SEDIMENT MOVEMENTS IN WATER INTAKES WITH MULTIBLOCK OPTION. 5007.
55. Rijn LC. Mathematical modelling of morphological processes in the case of

suspended sediment transport. Waterloopkundig Laboratorium; 1987.
56. Harlow FH, Nakayama PI. Turbulence transport equations. The Physics of Fluids. 1967 Nov 1;10(11):2323-32.
57. Launder BE, Spalding DB. Mathematical models of turbulence, text book.
58. Shirali S, Masjedi A. Control of sediment at lateral intake with using submerged vanes in river bend. Water Resources Engineering. 2018 Aug 23;11(37):13-22.
59. Odgaard AJ. River training and sediment management with submerged vanes. American Society of Civil Engineers. 2009.
60. Baduna Koçyiğit M, Koçyiğit Ö. Experimental Investigation of Bridge Scour under Pressure Flow Conditions. Water. 2024 Sep 29;16(19):2773.
61. Neary VS, Odgaard AJ. Three-dimensional flow structure at open-channel diversions. Journal of Hydraulic Engineering. 1993 Nov;119(11):1223-30.
62. Shaheed R, Mohammadian A, Yan X. A review of numerical simulations of secondary flows in river bends. Water. 2021 Mar 24;13(7):884.
63. Brethouwer G. Turbulent flow in curved channels. Journal of Fluid Mechanics. 2022 Jan;931:A21.
64. Odgaard AJ, Kennedy JF. River-bend bank protection by submerged vanes. Journal of hydraulic engineering. 1983 Aug;109(8):1161-73.
65. Neary VS, Sotiropoulos F, Odgaard AJ. Three-dimensional numerical model of lateral-intake inflows. Journal of Hydraulic Engineering. 1999 Feb;125(2):126-40.
66. Davoodi L, Shafai Bejestan M. Application of submerged vanes for sediment control at Intakes from Irrigation trapezoidal channels. Water and Irrigation Management. 2012 Feb 20;1(2):59-71.
67. Montaseri H, Godsian M, Salehi Neyshabouri SAA. Experimental study on design parameters of submerged vanes for sediment control at lateral intake in a 180 degree bend. Modares Civil Engineering journal. 2020 20(1): 161-176 (In Persian).
68. Fahmy WA, Ali AM, El-Bahlol MN, Ibrahim MM, Samy A. Enhancing baffle columns' performance to mitigate sedimentation at intake structures. Applied Water Science. 2024 May;14(5):89.
69. Ezz-Aldeen M, Al-Ansari N, Abd-Albaki Y, Knutsson S, Laue J. Sediment control strategies for sustainable water intake. Dams and Reservoirs. 2021 Mar;31(1):21-30.

© 2025 by the authors. Licensee SCU, Ahvaz, Iran. This article is an open access article distributed under the terms and conditions of the Creative Commons Attribution 4.0 International (CC BY 4.0 license) (http://creativecommons.org/licenses/by/4.0/).

Appendix


(a)
Intake Connection Location
Maximum 0.182621 m/s
Minimum 0.025186 m/s.
Maximum 0.140612 m/s
Minimum 0.008705 m/s,
(b)
Intake Connection Location
Maximum 0.212410 m/s
Minimum 0.028892 m/s,
Maximum 0.149307 m/s
Minimum 0.007175 m/s,


(c)
Intake Connection Location
Maximum 0.214756 m/s
Minimum 0.062476 m/s,
Maximum 0.151494 m/s
Minimum 0.007771 m/s.
(d)
Intake Connection Location
Maximum 0.211104 m/s
Minimum 0.075520 m/s,
Maximum 0.152494 m/s
Minimum 0.004927 m/s,

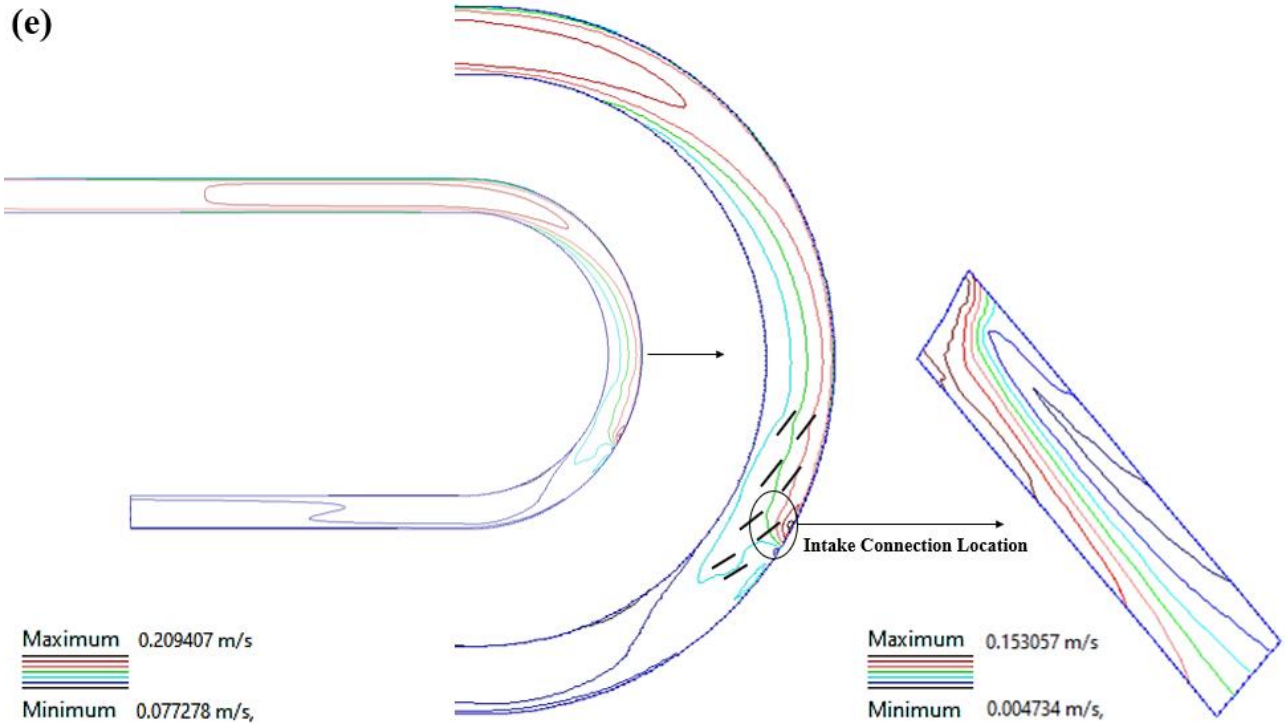
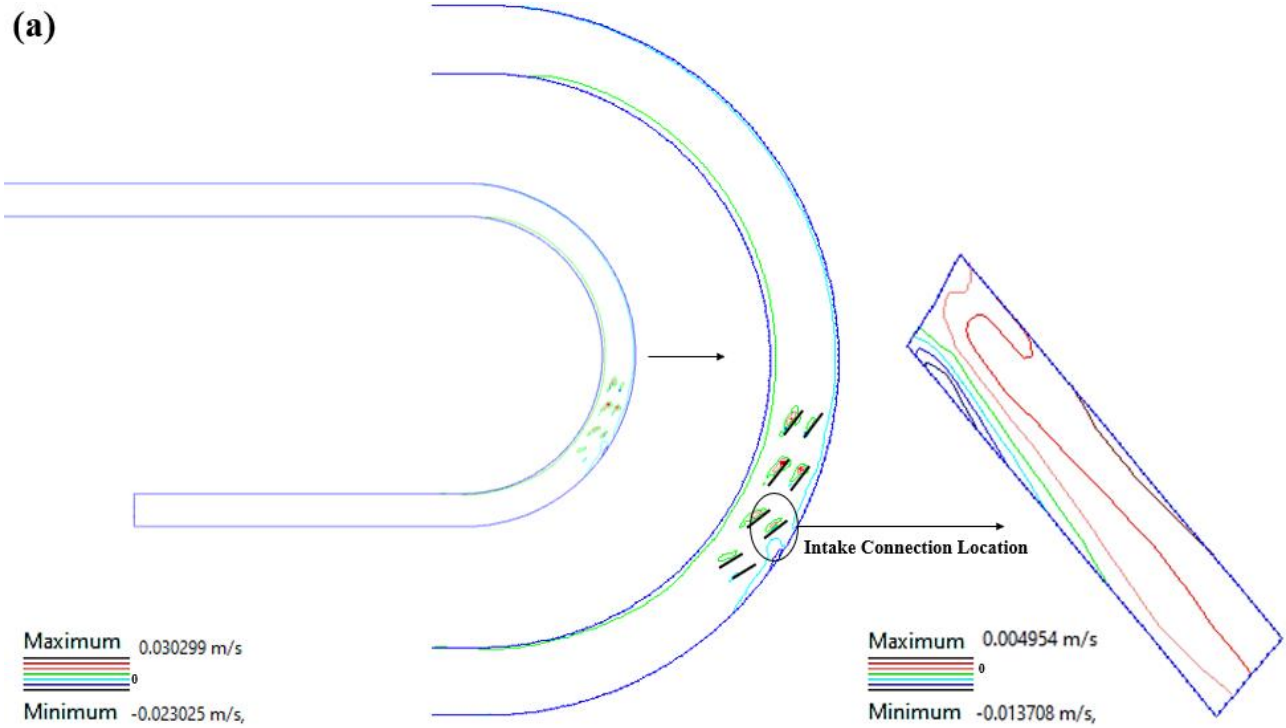
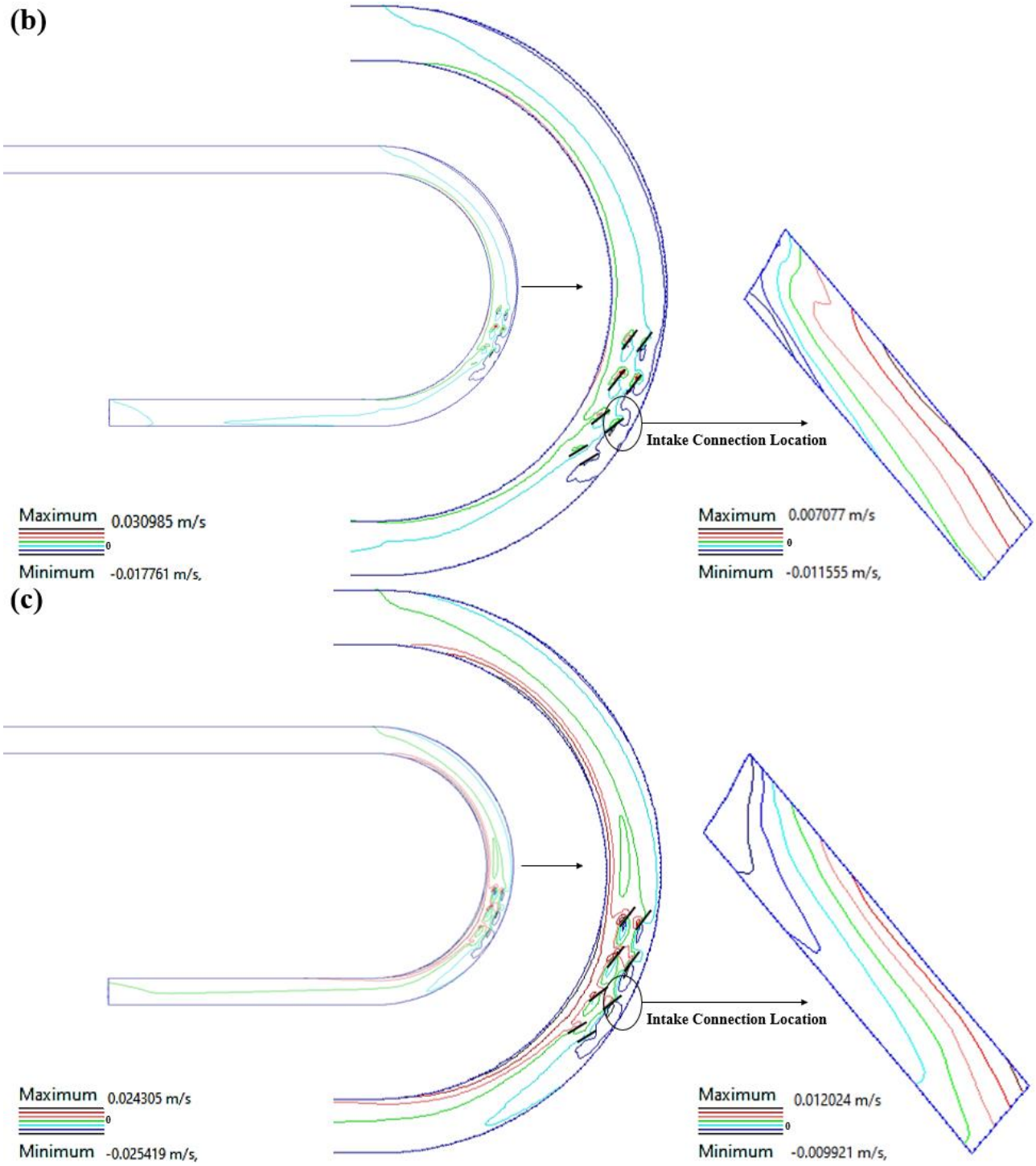


Fig. App.1 Stream-wise velocities in main channel and intake (Vane Length is 15cm) a) h/y=0, b) h/y=0.3, c) h/y=0.6, d) h/y=0.8, e) h/y=0.975




(b)
Intake Connection Location
Maximum 0.030985 m/s
0
Minimum -0.017761 m/s,
Maximum 0.007077 m/s
0
Minimum -0.011555 m/s,
(c)
Intake Connection Location
Maximum 0.024305 m/s
0
Minimum -0.025419 m/s,
Maximum 0.012024 m/s
0
Minimum -0.009921 m/s,

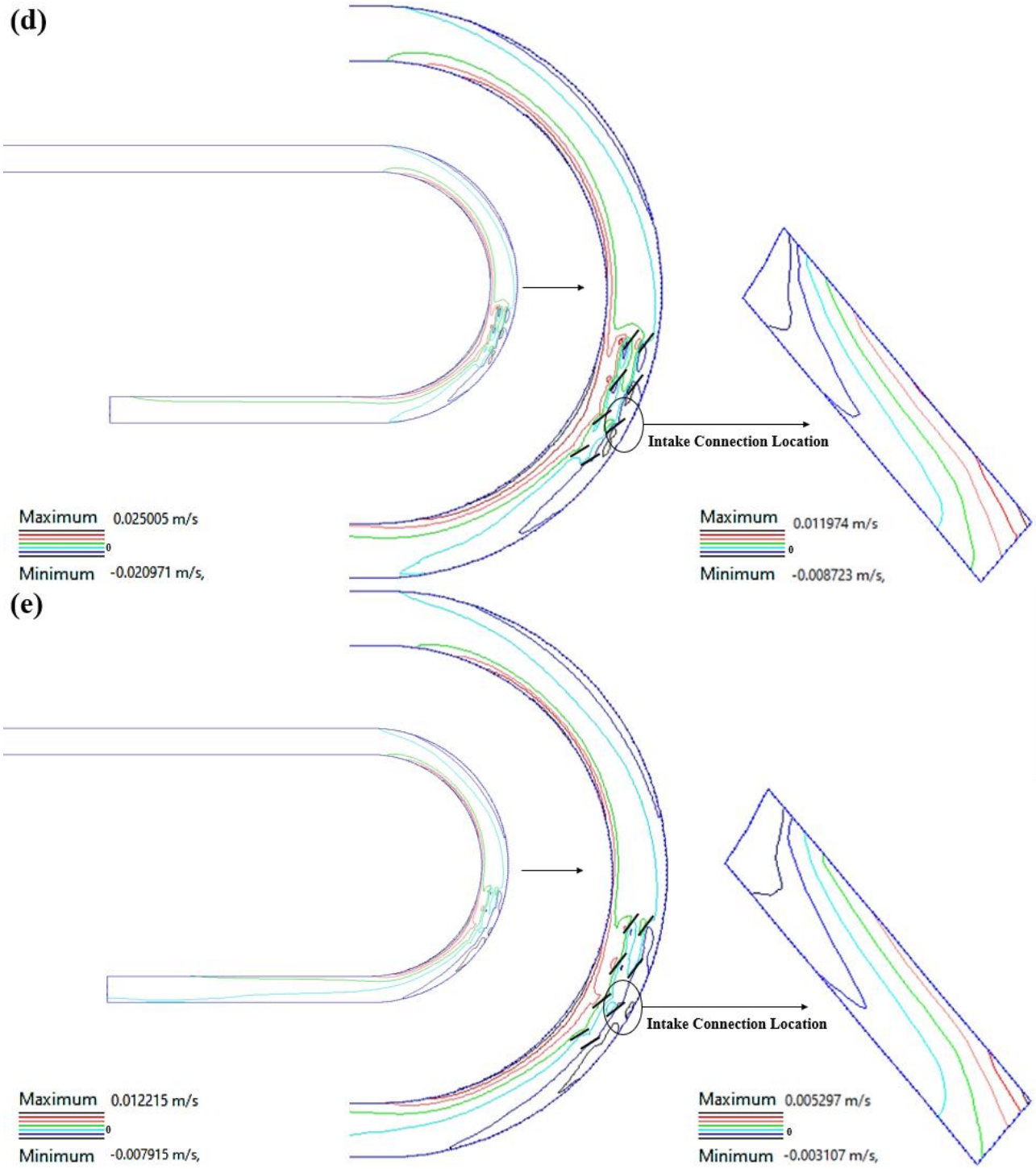
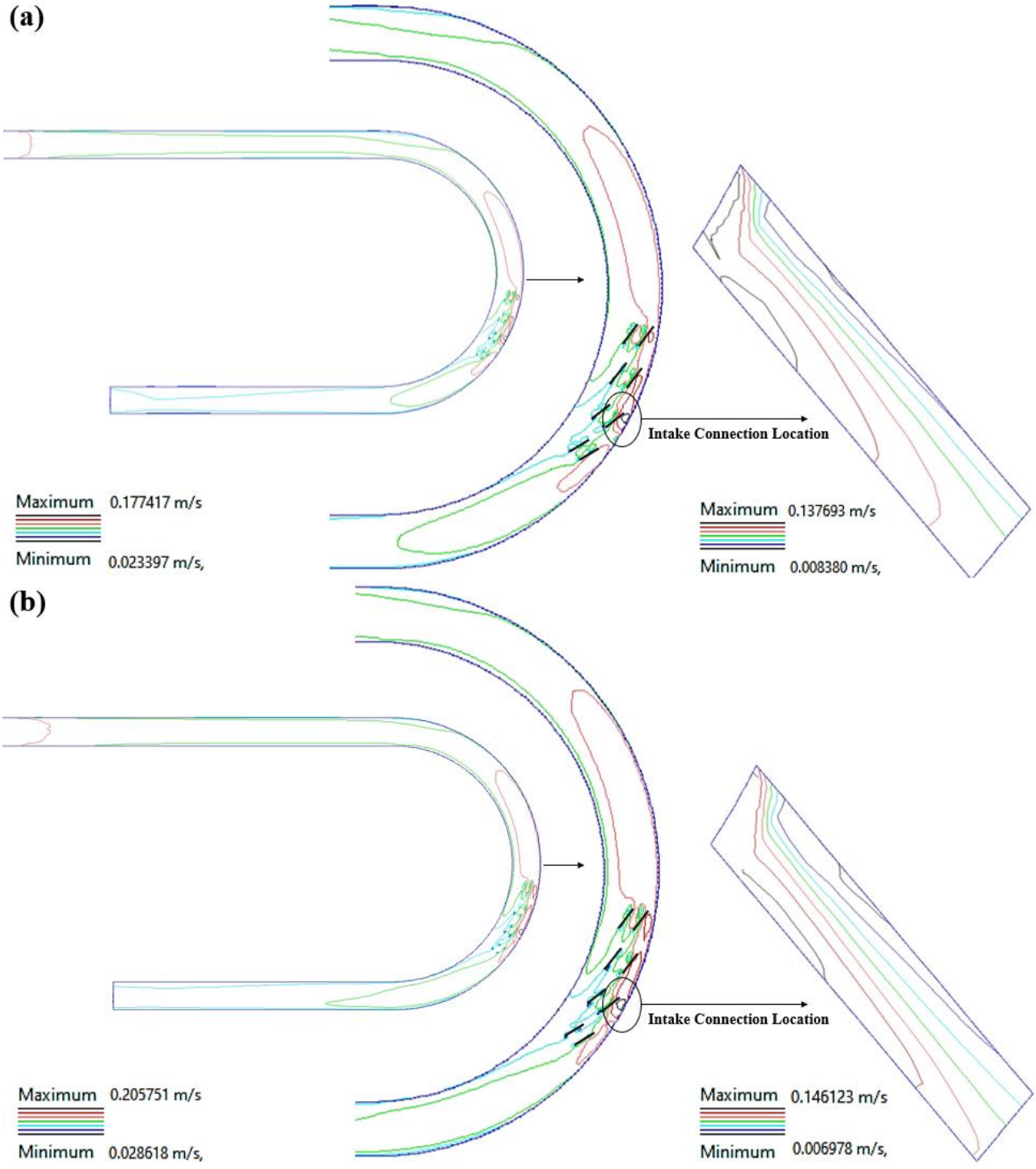
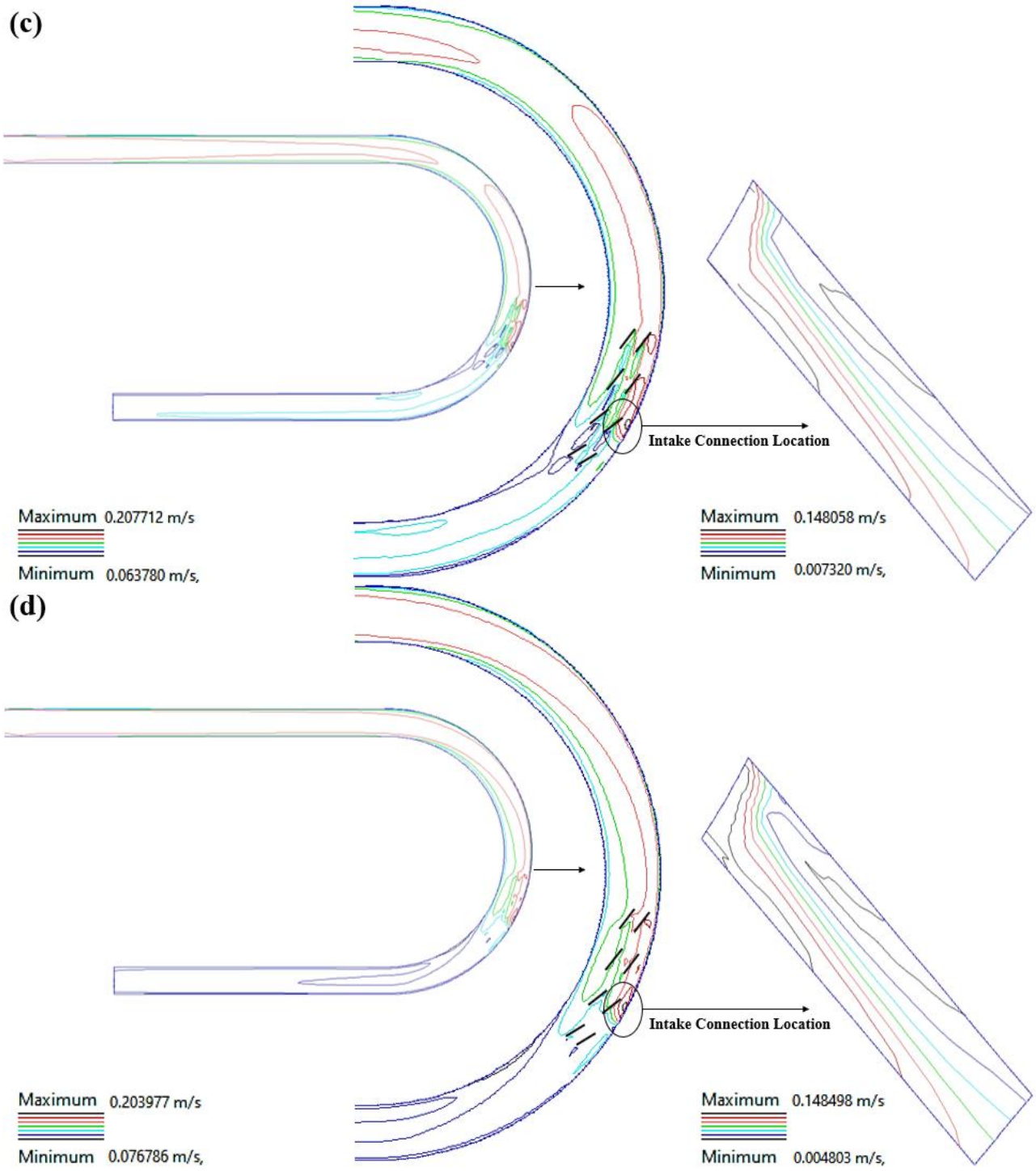


Fig. App.2 Vertical velocities in main channel and intake (Vane Length is 15cm) a) h/y=0, b) h/y=0.3, c) h/y=0.6, d) h/y=0.8, e) h/y=0.975

A.1. Influence of the transverse distance of Vanes




(c)
Intake Connection Location
Maximum 0.207712 m/s
Minimum 0.063780 m/s,
Maximum 0.148058 m/s
Minimum 0.007320 m/s,
(d)
Intake Connection Location
Maximum 0.203977 m/s
Minimum 0.076786 m/s,
Maximum 0.148498 m/s
Minimum 0.004803 m/s,

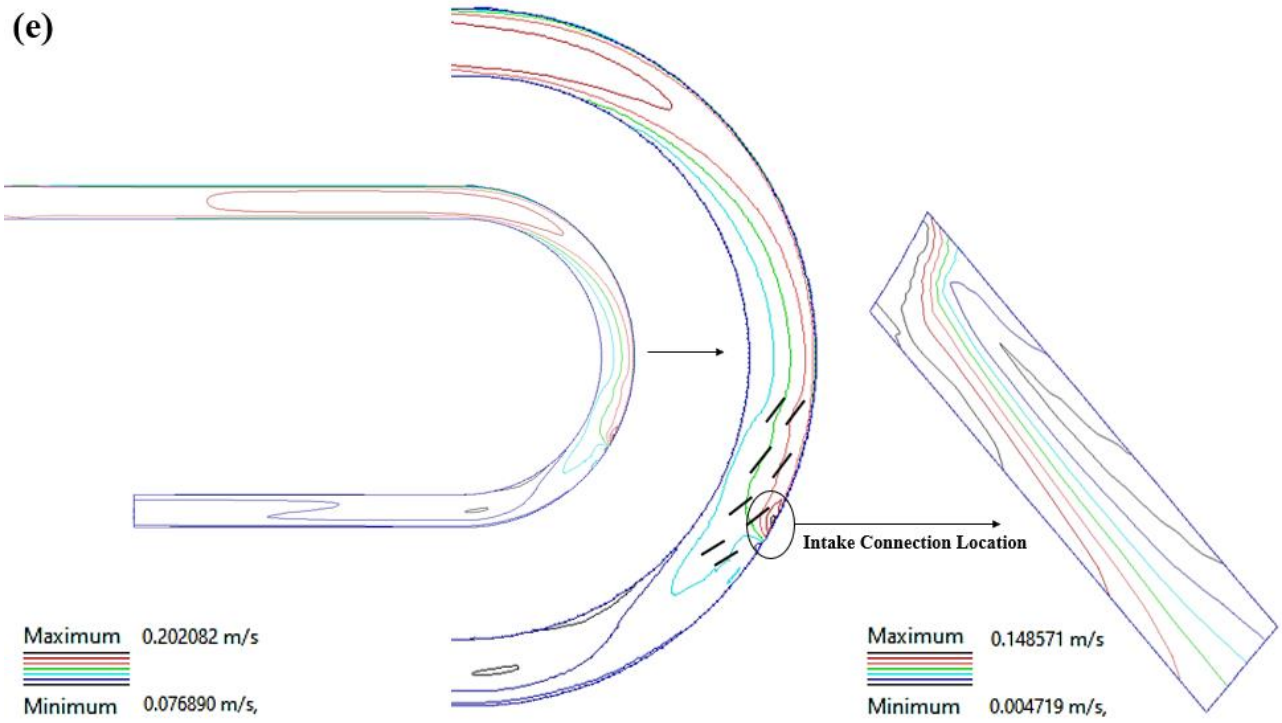
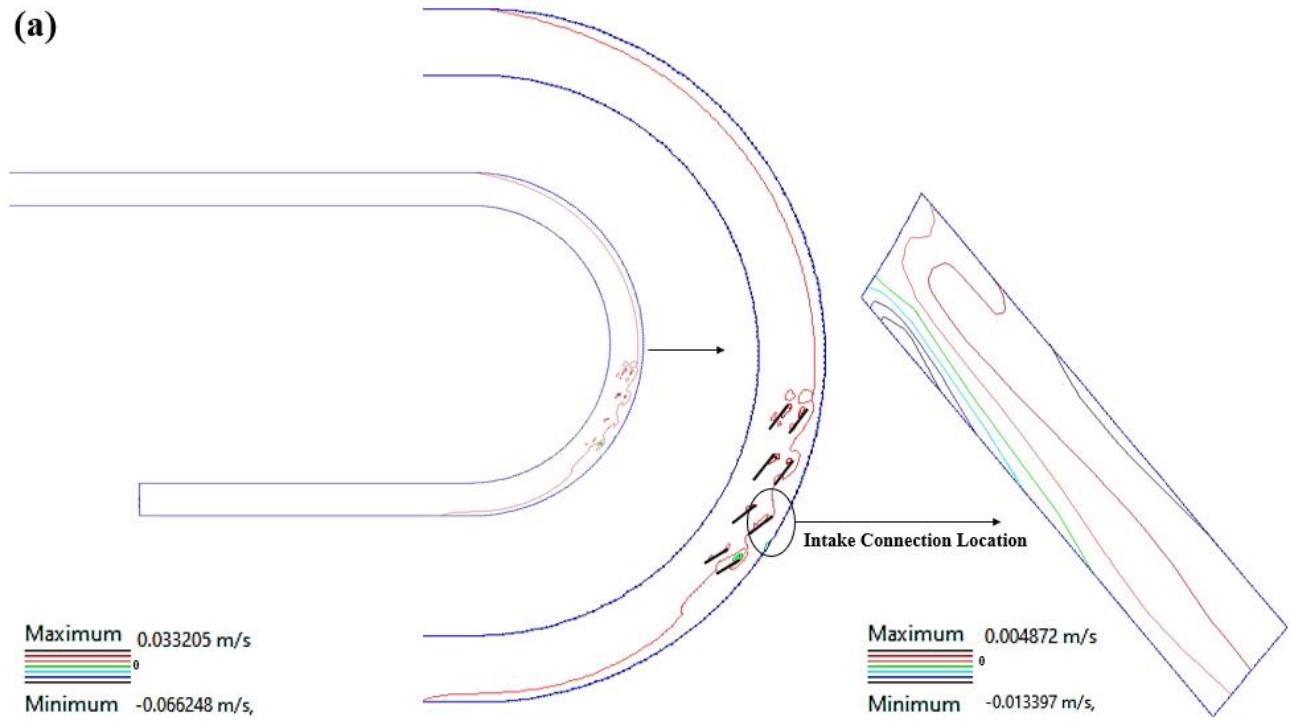
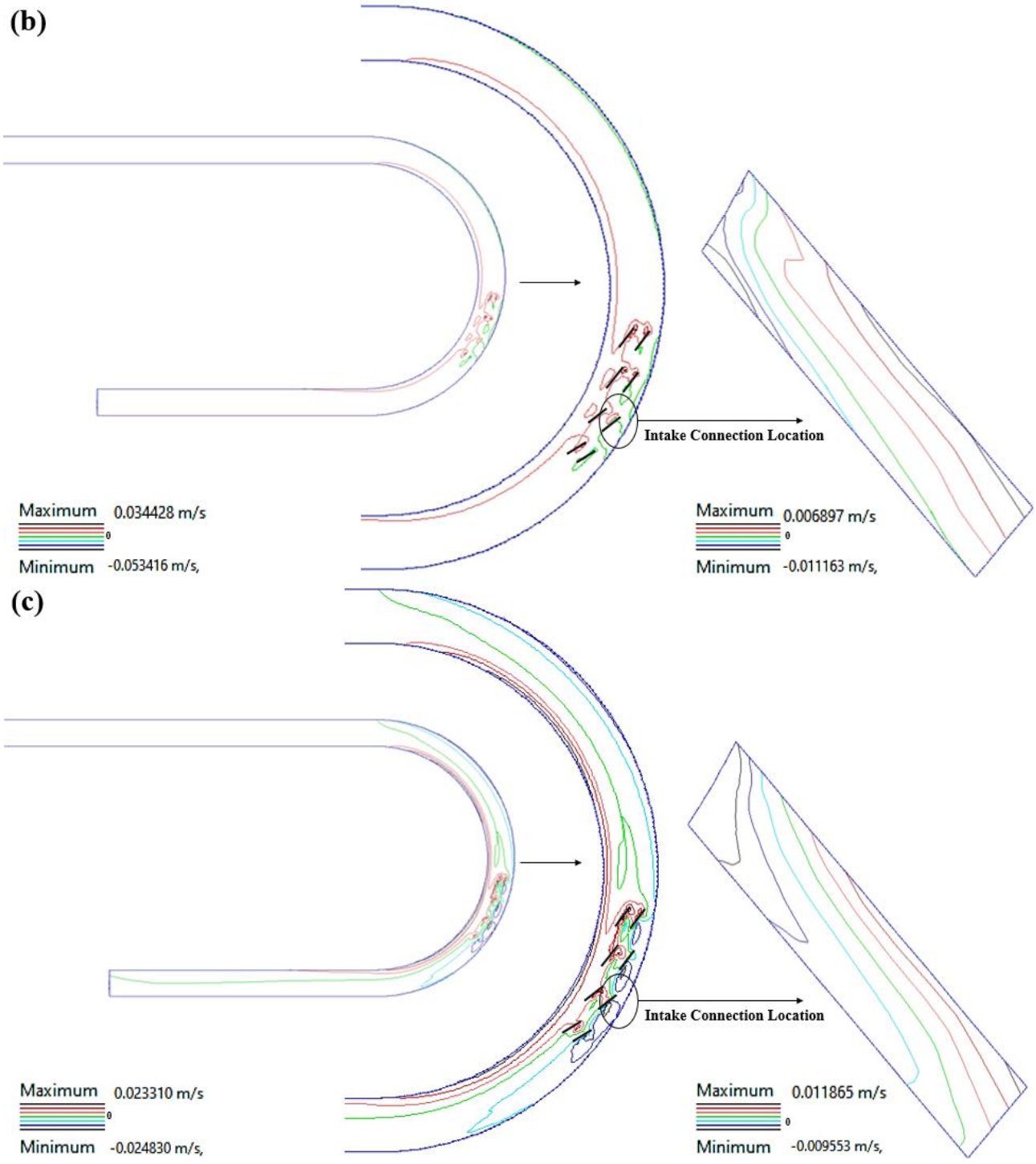


Fig. App.3 Stream-wise velocities in main channel and intake (transverse distance of Vanes is 13cm) a) h/y=0, b) h/y=0.3, c) h/y=0.6, d) h/y=0.8, e) h/y=0.975




(b)
Intake Connection Location
Maximum 0.034428 m/s
0
Minimum -0.053416 m/s,
Maximum 0.006897 m/s
0
Minimum -0.011163 m/s,
(c)
Intake Connection Location
Maximum 0.023310 m/s
0
Minimum -0.024830 m/s,
Maximum 0.011865 m/s
0
Minimum -0.009553 m/s,

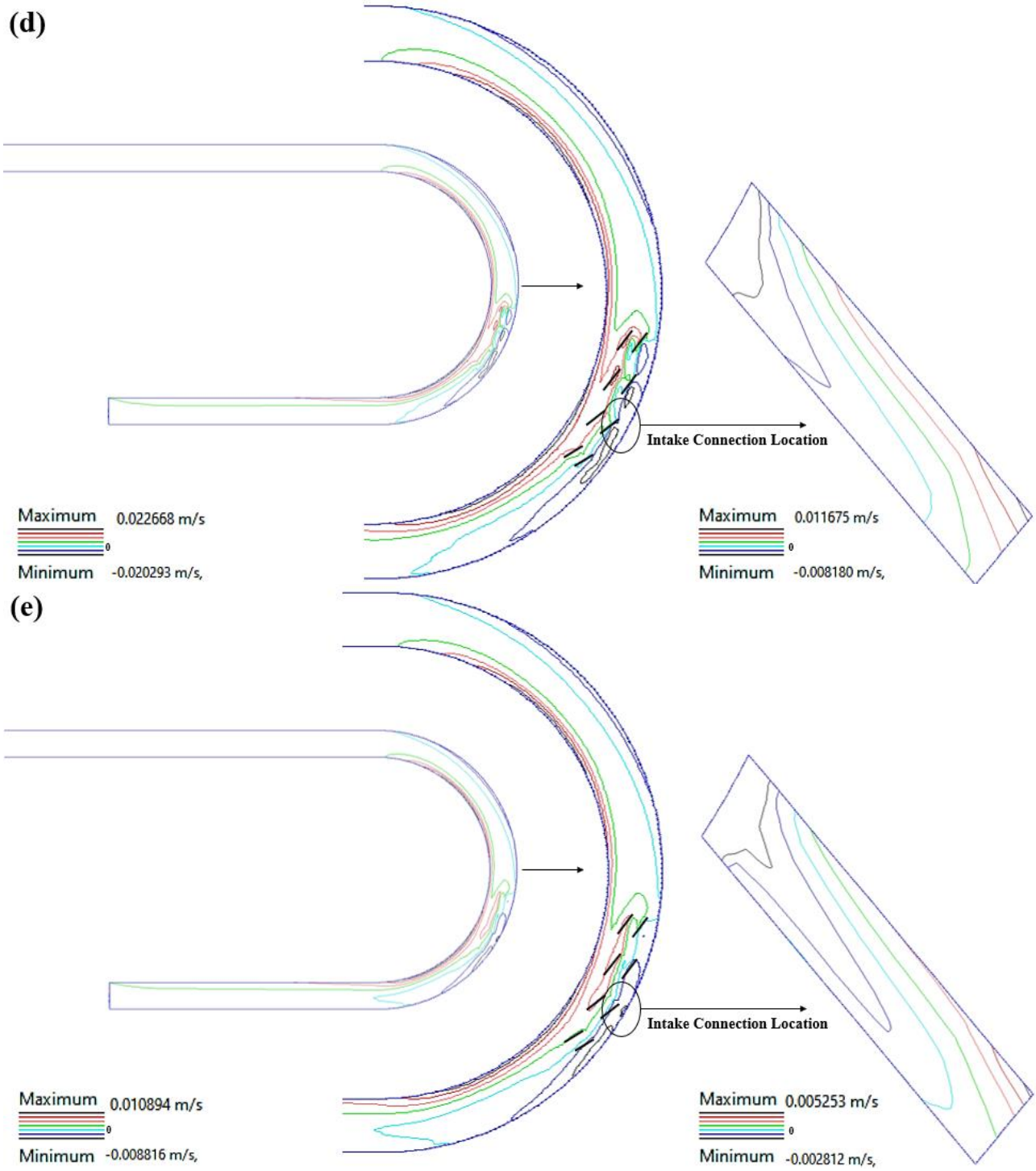
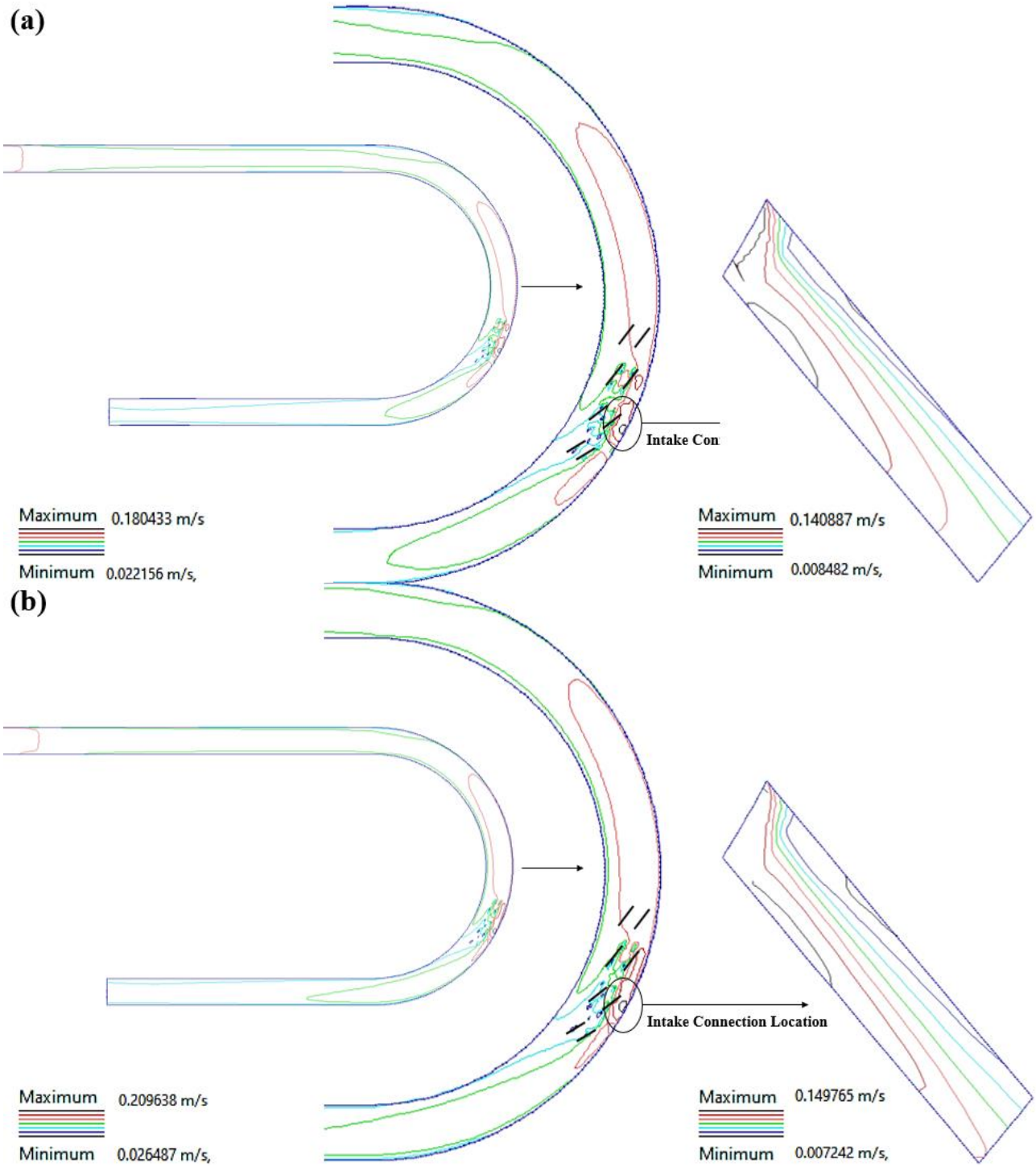
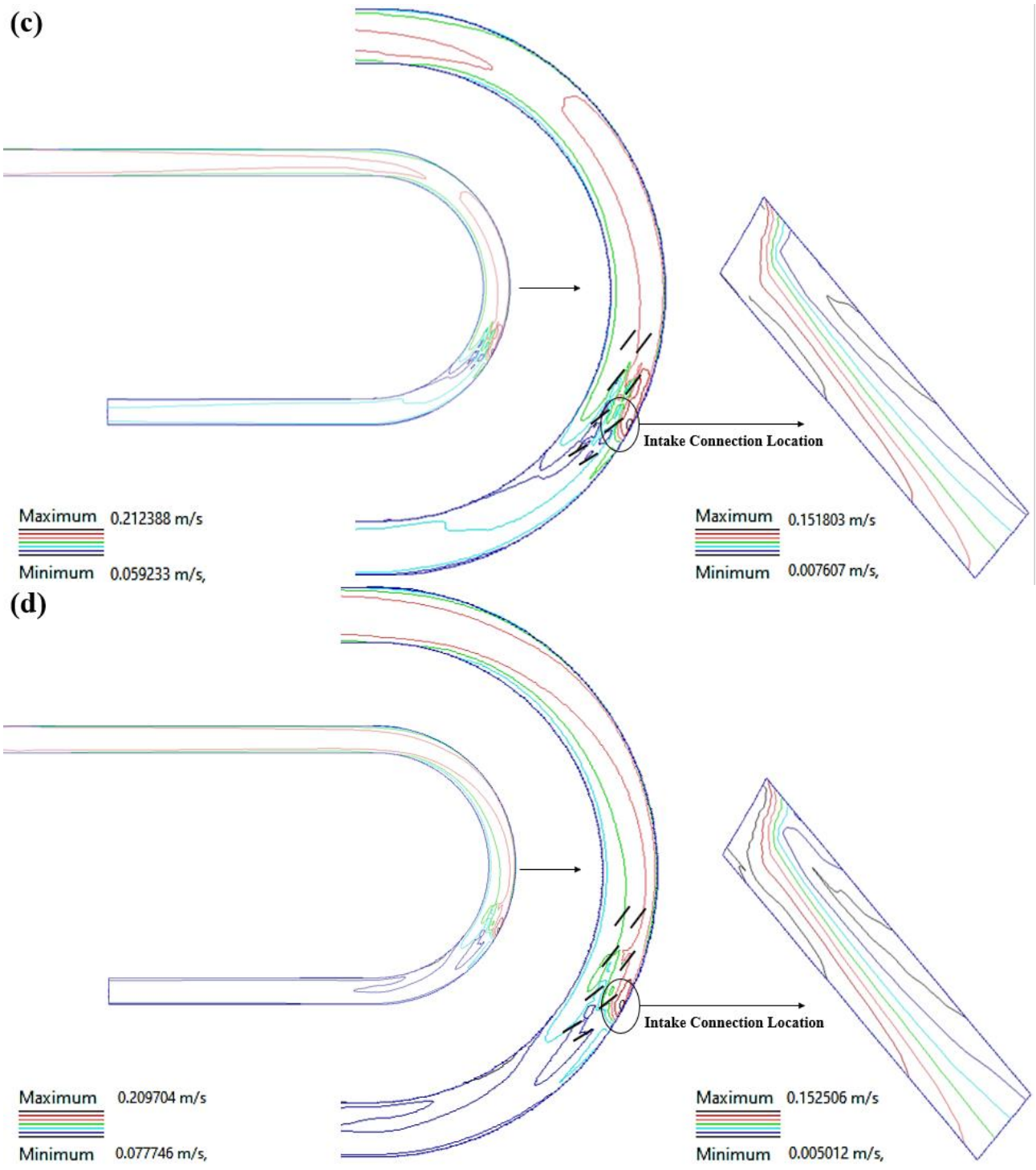


Fig. App.4 Vertical velocities in main channel and intake (transverse distance of Vanes is 13cm) a) h/y=0, b) h/y=0.3, c) h/y=0.6, d) h/y=0.8, e) h/y=0.975

A.2. Influence of the Longitudinal Distance of Vanes


(a)
Intake Con
Maximum 0.180433 m/s
Minimum 0.022156 m/s,
Maximum 0.140887 m/s
Minimum 0.008482 m/s,
(b)
Intake Connection Location
Maximum 0.209638 m/s
Minimum 0.026487 m/s,
Maximum 0.149765 m/s
Minimum 0.007242 m/s,


(c)
Intake Connection Location
Maximum 0.212388 m/s
Minimum 0.059233 m/s,
Maximum 0.151803 m/s
Minimum 0.007607 m/s,
(d)
Intake Connection Location
Maximum 0.209704 m/s
Minimum 0.077746 m/s,
Maximum 0.152506 m/s
Minimum 0.005012 m/s,

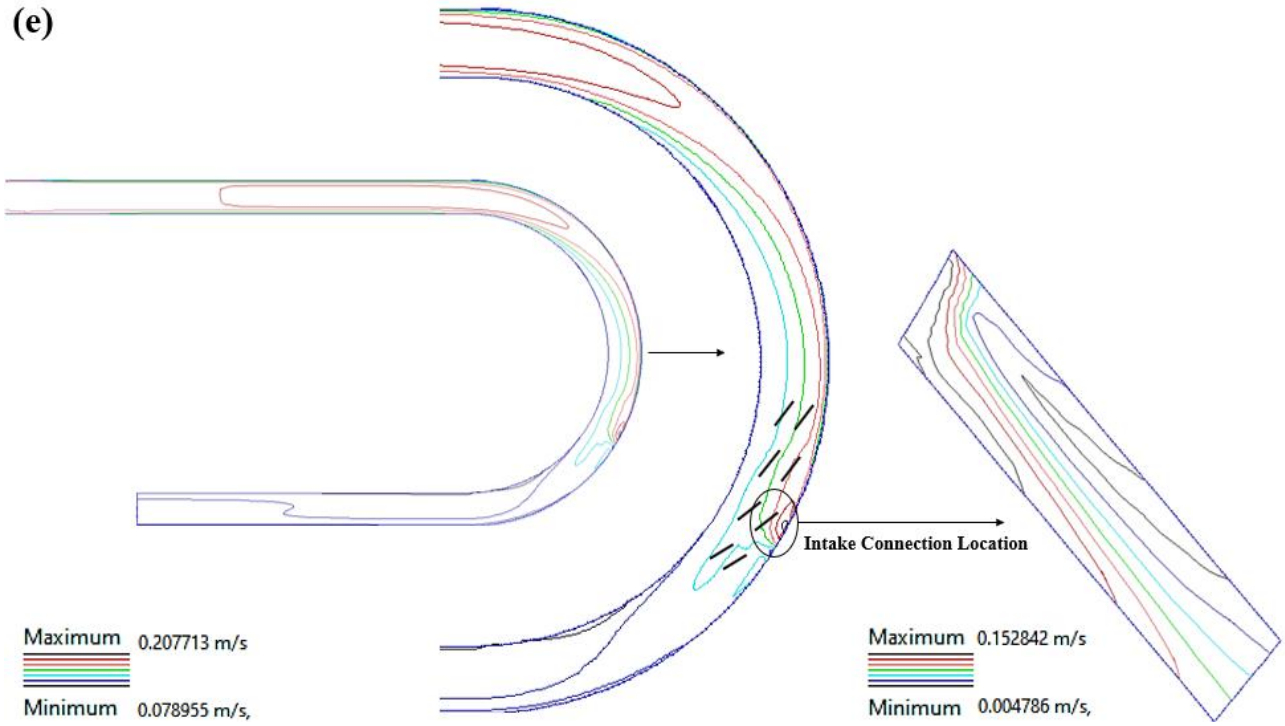
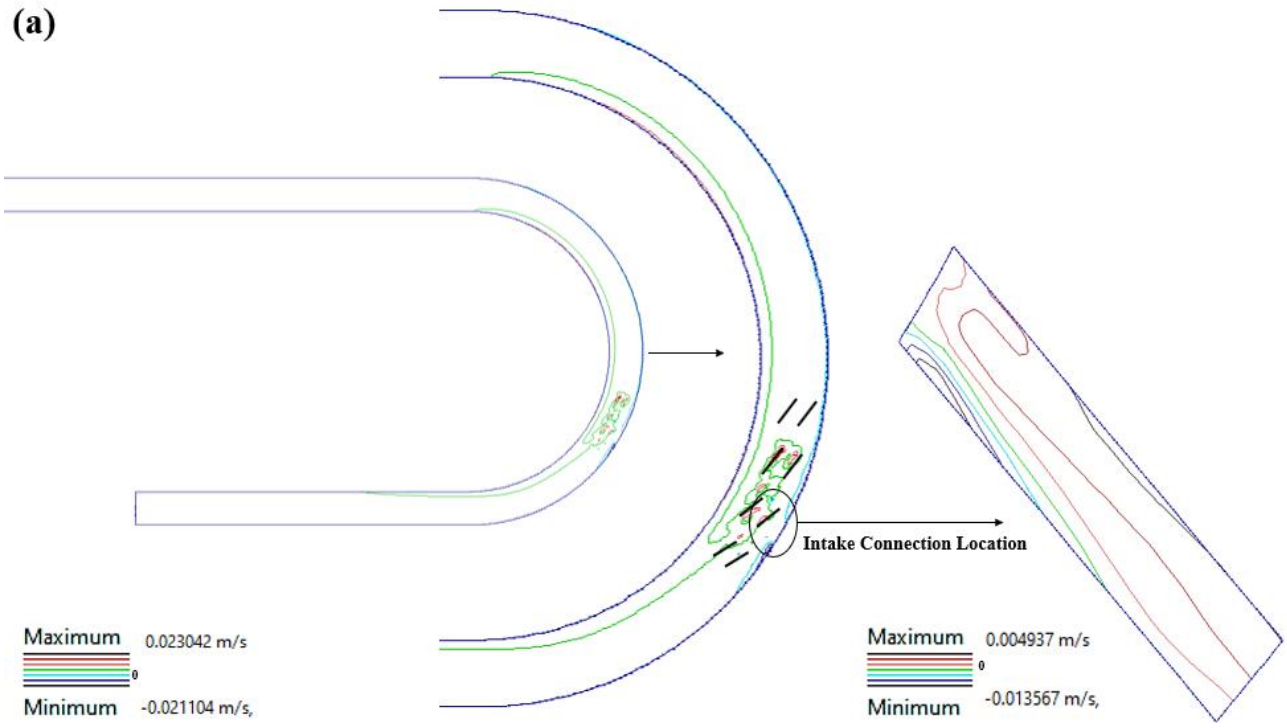
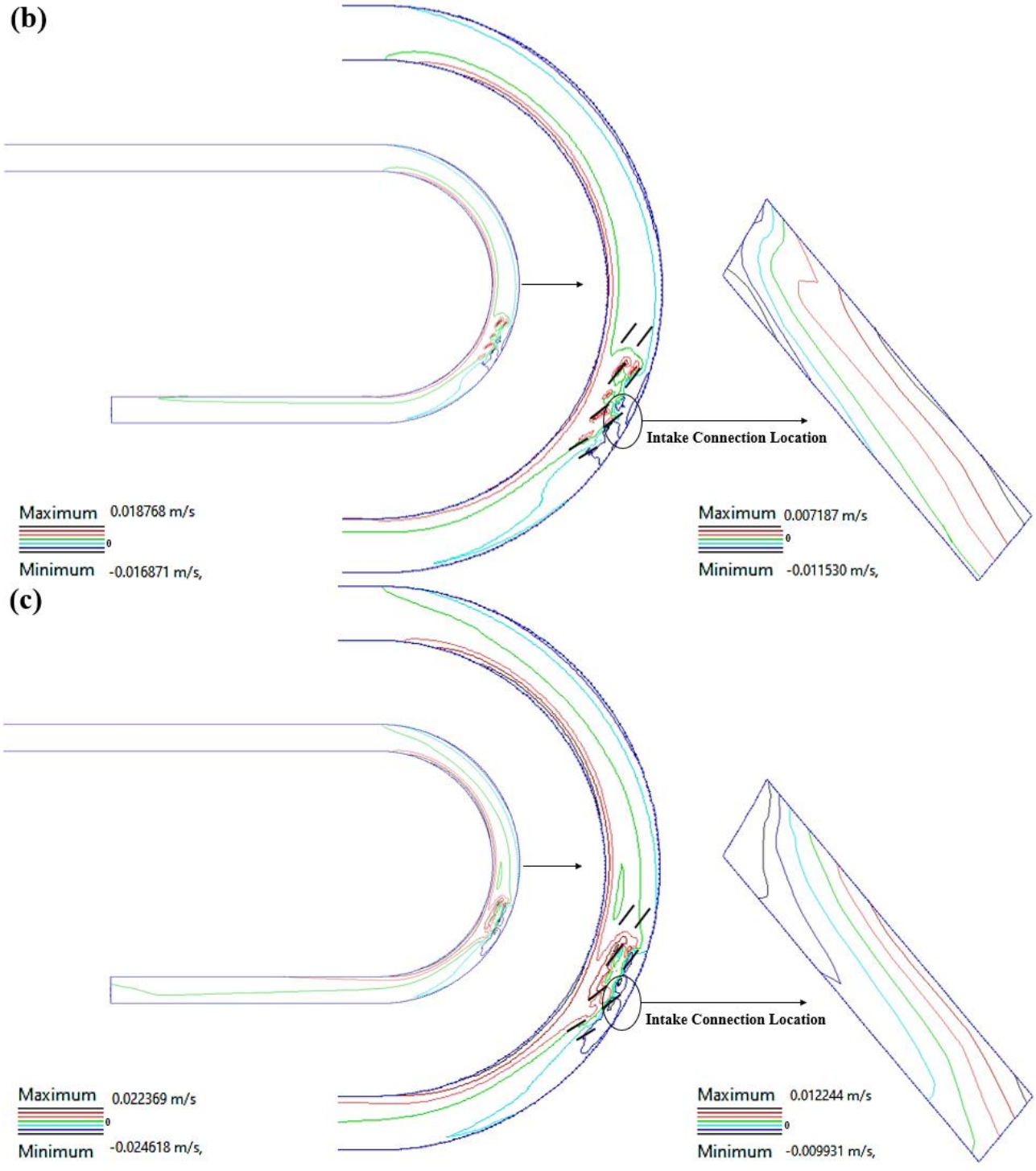


Fig. App.5 Stream-wise velocities in main channel and intake (longitudinal distance of Vanes is 30cm) a) h/y=0, b) h/y=0.3, c) h/y=0.6, d) h/y=0.8, e) h/y=0.975




(b)
Intake Connection Location
Maximum 0.018768 m/s
0
Minimum -0.016871 m/s,
Maximum 0.007187 m/s
0
Minimum -0.011530 m/s,
(c)
Intake Connection Location
Maximum 0.022369 m/s
0
Minimum -0.024618 m/s,
Maximum 0.012244 m/s
0
Minimum -0.009931 m/s,

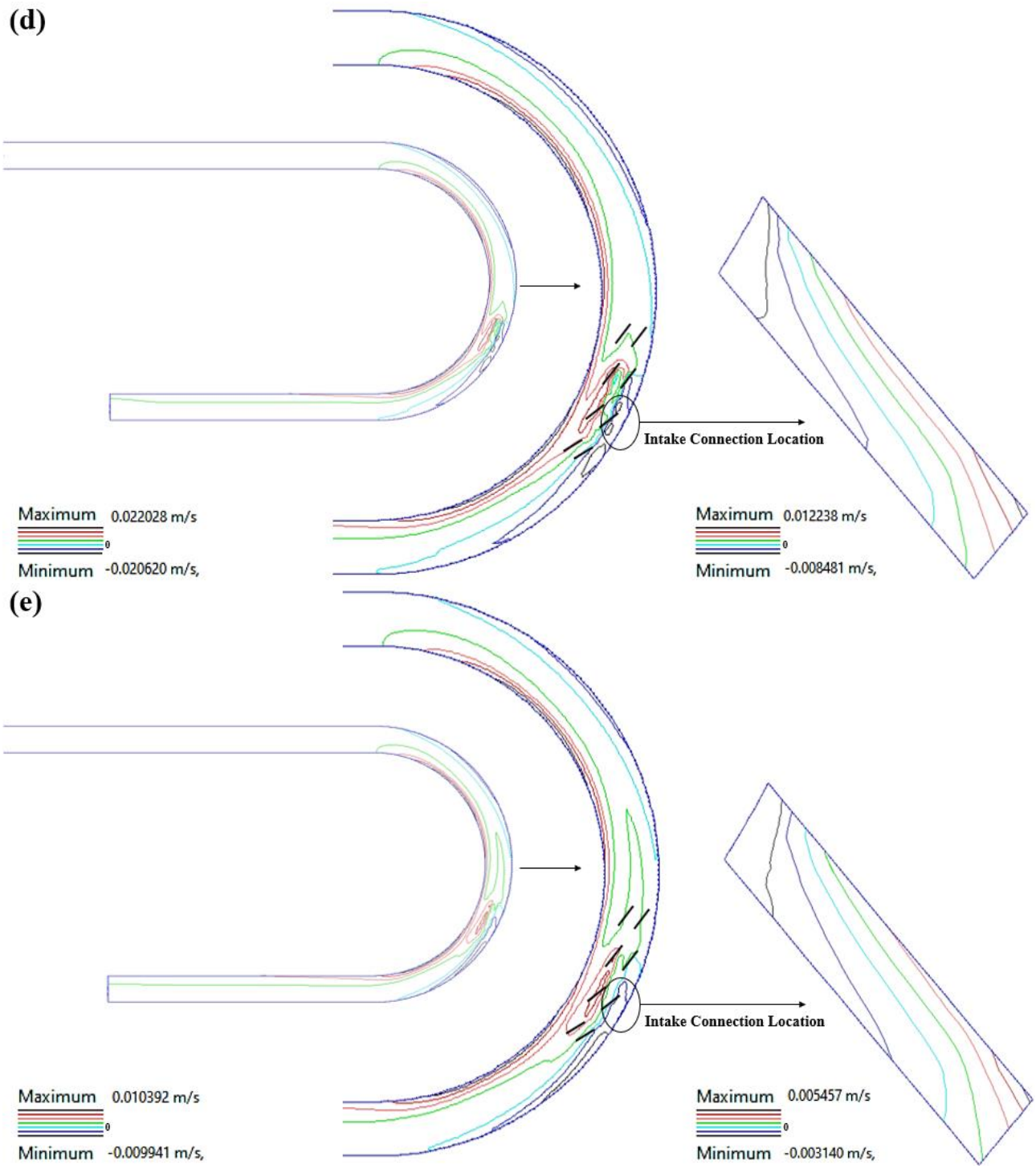
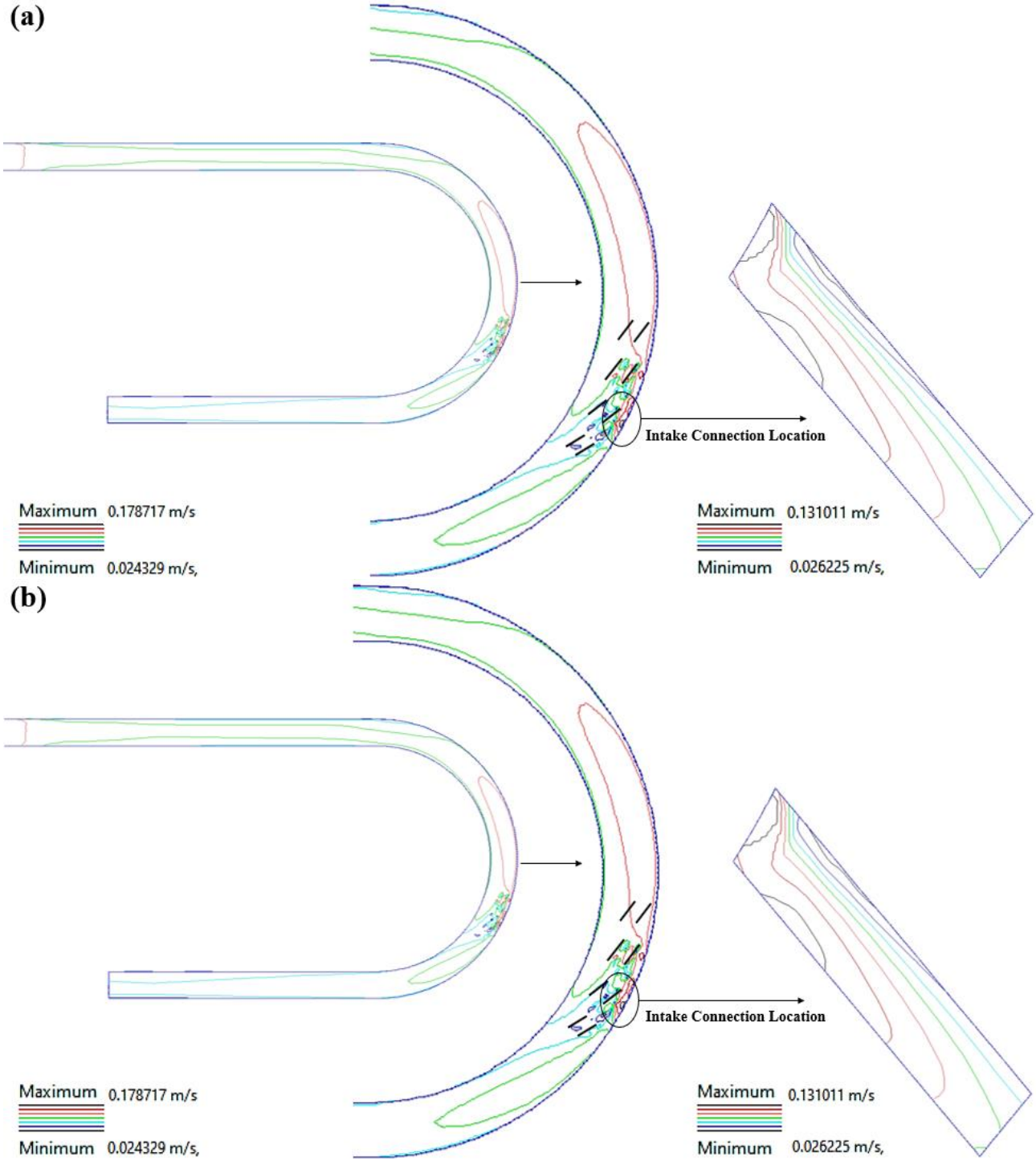
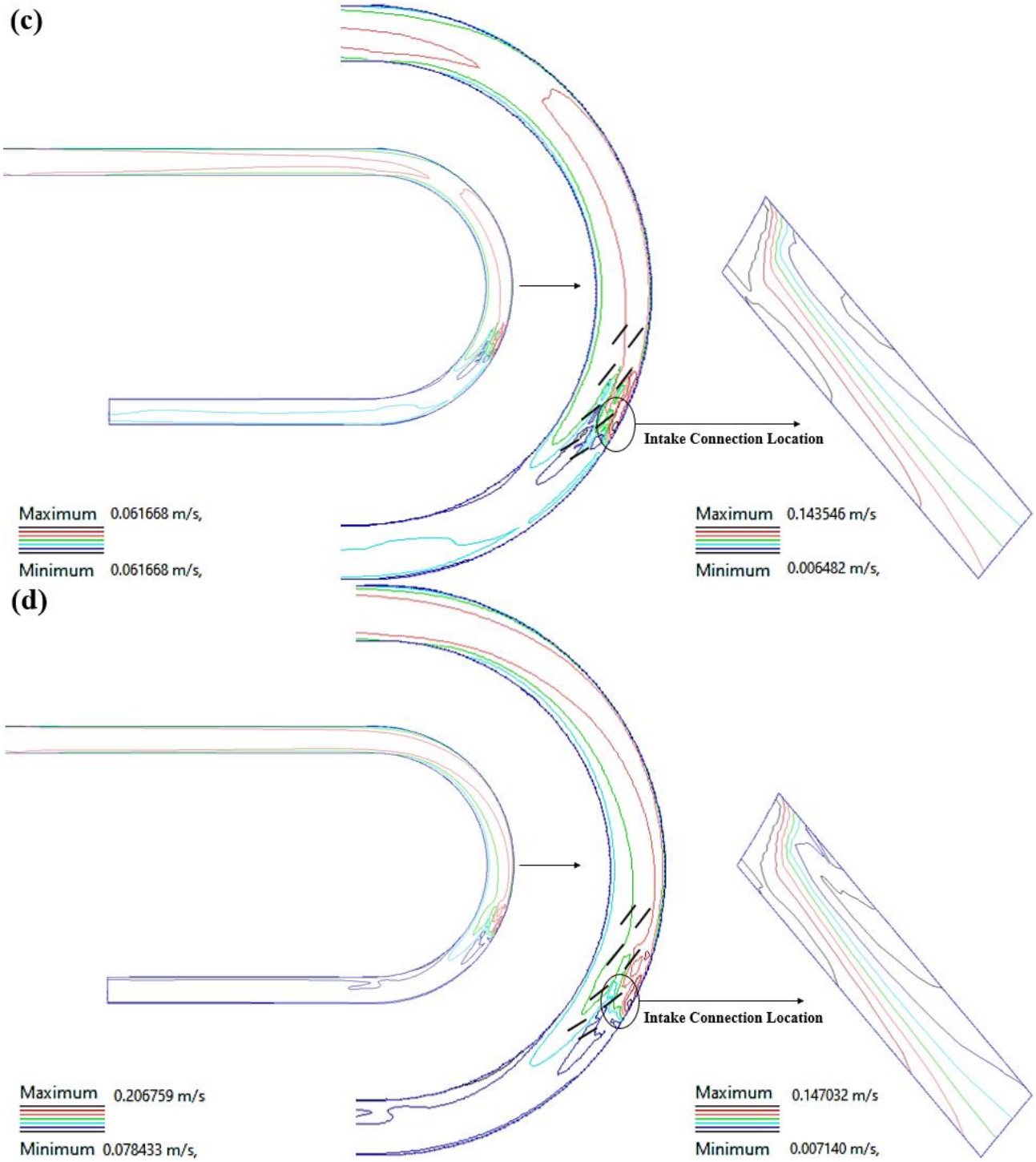


Fig. App.6 Vertical velocities in main channel and intake (longitudinal distance of Vanes is 30cm) a) h/y=0, b) h/y=0.3, c) h/y=0.6, d) h/y=0.8, e) h/y=0.975

A.3. Influence of the distance of the first row from the intake




(c)
Intake Connection Location
Maximum 0.061668 m/s,
Minimum 0.061668 m/s,
Maximum 0.143546 m/s
Minimum 0.006482 m/s,
(d)
Intake Connection Location
Maximum 0.206759 m/s
Minimum 0.078433 m/s,
Maximum 0.147032 m/s
Minimum 0.007140 m/s,

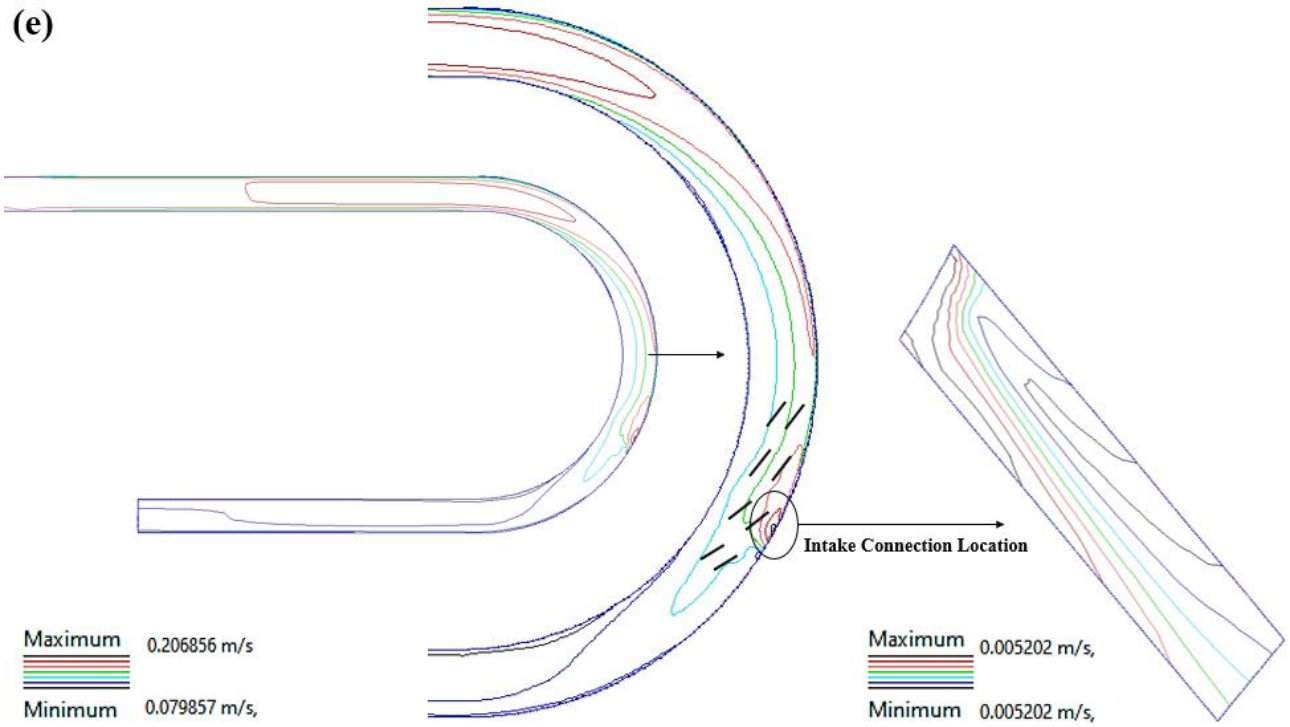
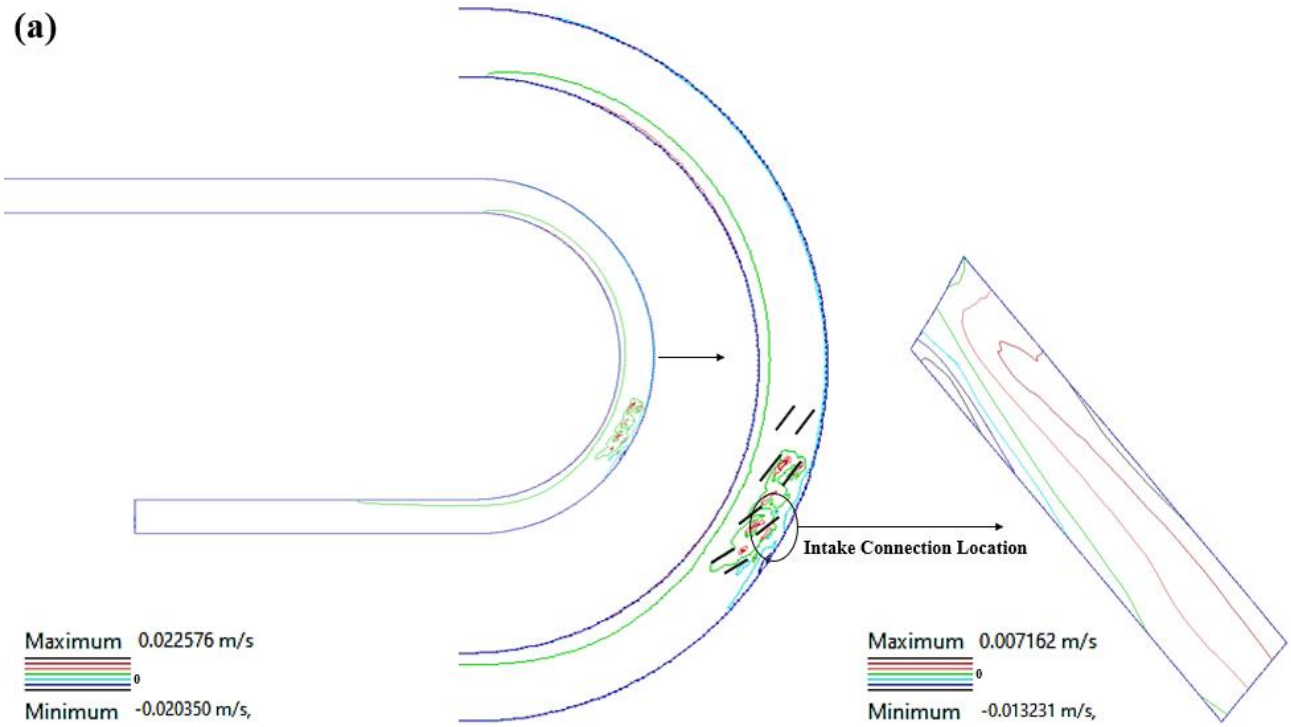
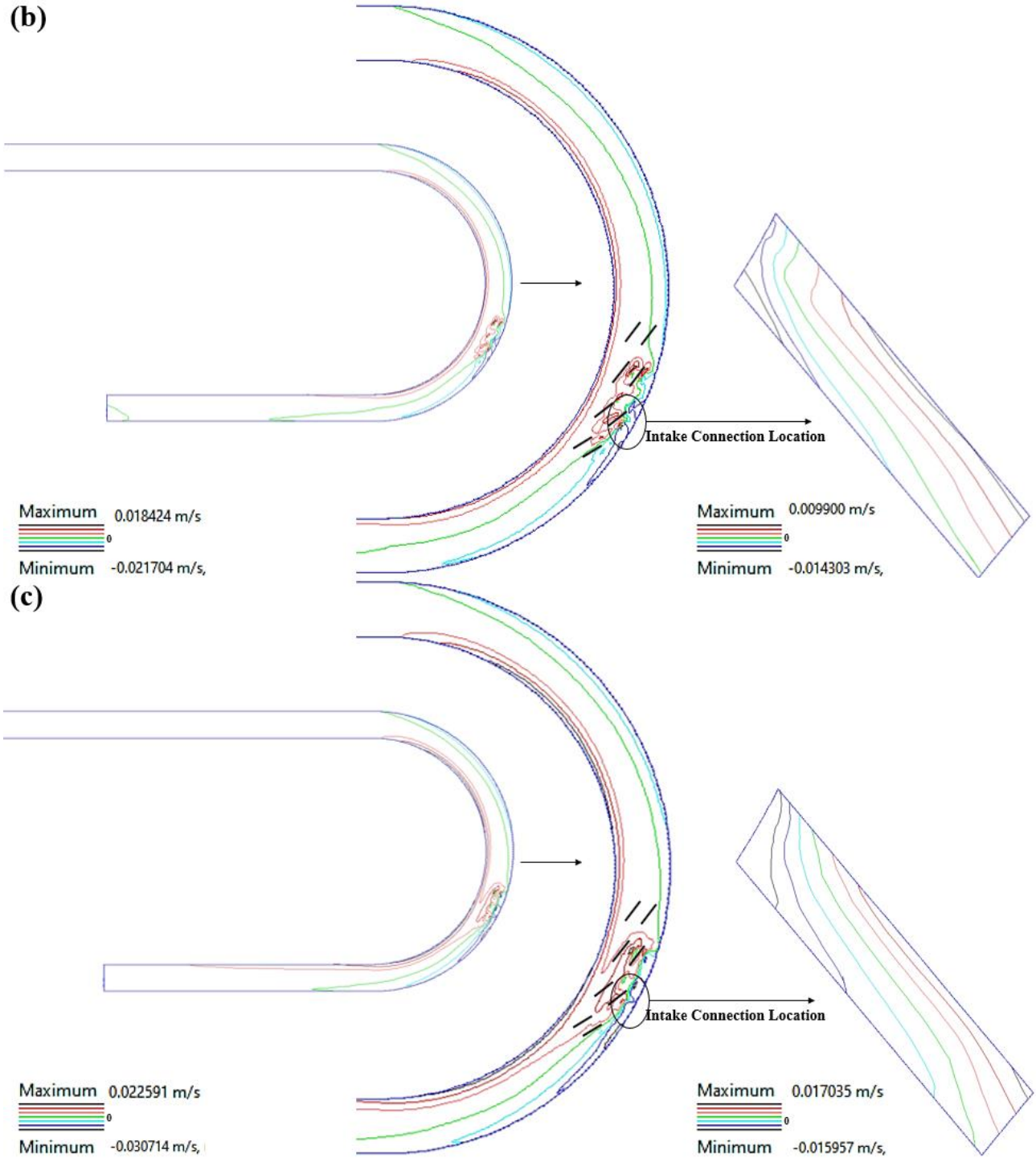


Fig. App.7 Stream-wise velocities in main channel and intake (distance of the first row from the intake is 12cm) a) h/y=0, b) h/y=0.3, c) h/y=0.6, d) h/y=0.8, e) h/y=0.975




(b)
Intake Connection Location
Maximum 0.018424 m/s
0
Minimum -0.021704 m/s,
Maximum 0.009900 m/s
0
Minimum -0.014303 m/s,
(c)
Intake Connection Location
Maximum 0.022591 m/s
0
Minimum -0.030714 m/s,
Maximum 0.017035 m/s
0
Minimum -0.015957 m/s,

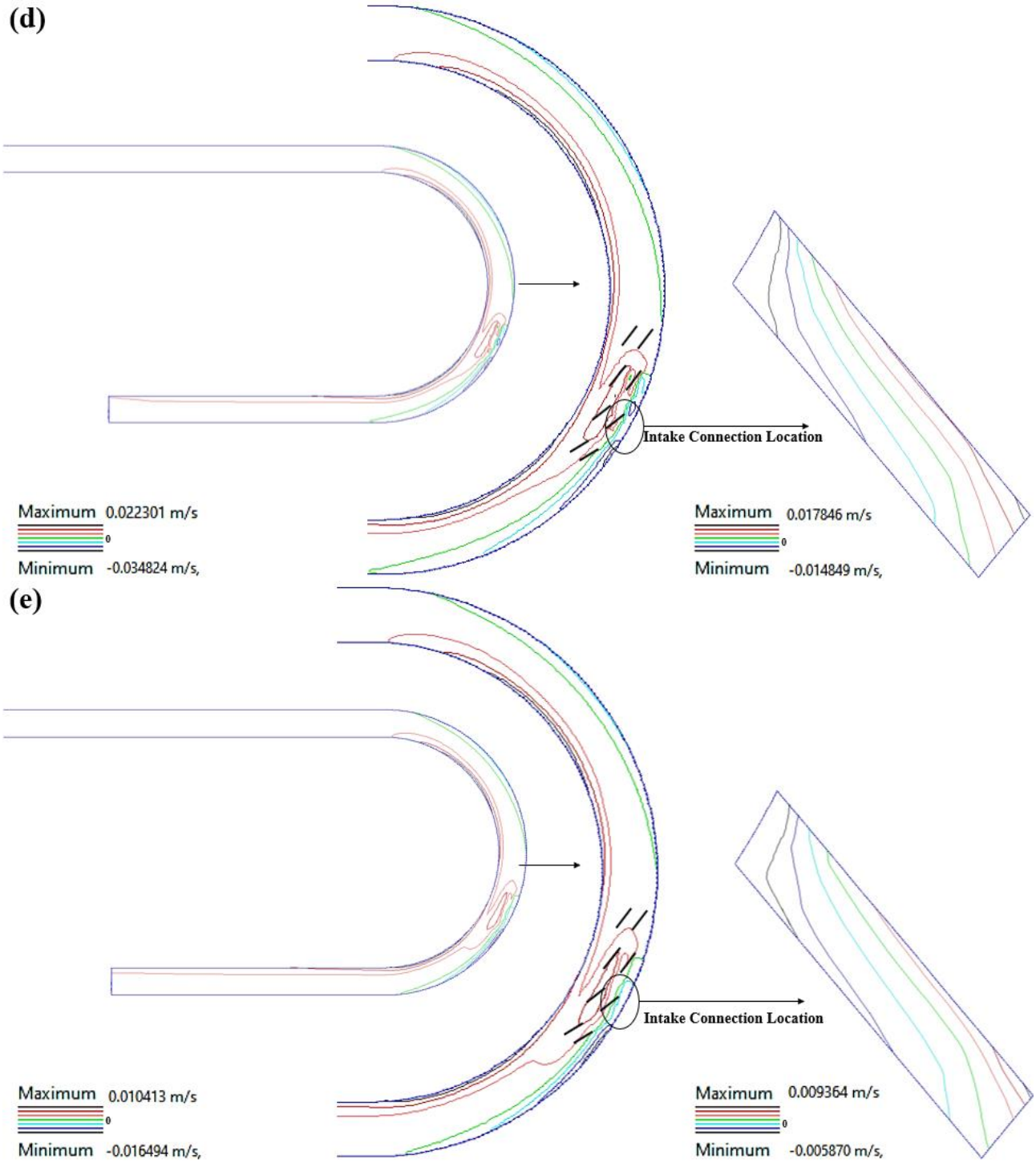


Fig. App.8 Vertical velocities in main channel and intake (distance of the first row from the intake is 12cm) a) h/y=0, b) h/y=0.3, c) h/y=0.6, d) h/y=0.8, e) h/y=0.975